Amyloid Beta Precursor Protein contributes to brain aging and learning decline in short-lived turquoise killifish (*Nothobranchius furzeri*)

Dennis E.M. de Bakker[a,b,c], Mihaela Mihaljević[b], Kunal Gharat[a], Yasmin Richter[d], Frauke van Bebber[e], Lisa Adam[a], Farzana Shamim-Schulze[a], Oliver Ohlenschläger[a], Martin Bens[a], Emilio Cirri[a], Adam Antebi[b,f], Ivan Matić[b], Anja Schneider[g], Bettina Schmid[e], Janine Kirstein[a,d], Dario Riccardo Valenzano[a,b,c,h,*]

[a]Leibniz Institute on Aging – Fritz Lipmann Institute (FLI), Beutenbergstrasse 11, 07745, Jena, Germany;

[b]Max Planck Institute for Biology of Ageing, Joseph-Stelzmann-Straße 9B, 50931 Cologne, Germany;

[c]Cluster of Excellence "Balance of the Microverse", Friedrich-Schiller-University, Jena, Germany;

[d]Friedrich-Schiller-University, Institute for Biochemistry and Biophysics, Hans-Knöll-Str. 2, 07745, Jena, Germany

[e]German Center for Neurodegenerative Diseases Munich, Feodor-Lynen-Str. 17, 81377, München, Germany;

[f]Cologne Excellence Cluster on Cellular Stress Responses in Aging-Associated Diseases (CECAD); University of Cologne, 50931, Cologne, Germany;

[g]German Center for Neurodegenerative Diseases, Venusberg-Campus 1/99, 53127 Bonn, Germany;

[h]Jena University Hospital/Friedrich-Schiller-University, Jena, Germany.

*corresponding author: dvalenzano@leibniz-fli.de

Abstract

Amyloid beta (Aβ) accumulation is associated with inflammation, neurodegeneration, and cognitive decline in the context of neurodegenerative diseases. However, its role during normal aging remains largely unexplored. In this study, we investigated the natural impact of Aβ precursor protein (*app*) on the aging brain using a short-lived vertebrate model, the turquoise killifish (*Nothobranchius furzeri*). We identified amyloid precursor protein derivatives in the killifish brain across different age groups and found that pyroglutamated amyloid beta —a neurotoxic Aβ variant—accumulates intra-neuronally in an age-dependent manner, co-localizing with the apoptosis marker TUNEL. To determine whether Aβ contributes to spontaneous brain aging, we used CRISPR/Cas9 to generate an "amyloid precursor protein a" (*appa*) knock-out killifish strain. Notably, *appa* -/- mutants exhibited reduced cell death and inflammation, an overall younger proteome, as well as improved learning capacity in old age. Taken together, we found that Aβ precursor protein broadly affects vertebrate brain aging, making it a promising target for anti-aging interventions.

Introduction

The aging brain undergoes several changes, including protein aggregation, inflammation, and neuronal loss. These changes are often exacerbated during neurodegenerative diseases, which possibly represent alternative aging trajectories[1–3]. Amyloid beta (Aβ) is a highly studied peptide that aggregates in the brain of healthy aging individuals as well as Alzheimer's disease (AD) patients[4,5]. Genetic and pharmacological induction of Aβ can drive neurodegenerative symptoms in worms[6,7], flies[8,9] and mice[10–12], and monoclonal antibodies and vaccination strategies targeting Aβ are being developed to slow down cognitive decline in AD patients[13–18]. However, whether Aβ plays a key role in normal aging and whether it can be targeted to reduce the degenerative brain phenotypes of the normal aging brain remains largely unexplored.

The investigation of the effect of spontaneous Aβ accumulation during aging requires an animal model whose natural aging trajectory includes both Aβ accumulation, as well as neurodegenerative phenotypes. Therefore, we set out to investigate the Aβ dynamics in a naturally short-lived vertebrate, which displays robust brain aging phenotypes, the turquoise killifish (*Nothobranchius furzeri*)[3]. Turquoise killifish have a median lifespan between three and eight months and rapidly develop a range of age-related phenotypes overlapping with human aging. These phenotypes include sarcopenia[19], cancer susceptibility[20], telomere attrition[21,22], impaired regenerative capacity[23,24], as well as a decrease in antibody diversity and increased immunosenescence[25–27]. Meanwhile, the killifish brain is subjected to age-related protein aggregation[28–32], astrogliosis[33,34], inflammation[24,34], neuronal degeneration[29,35–37] and reduced neurogenic potential[24,33,34], which together might be leading to a decreased learning capacity[37–39]. Considering that these brain aging phenotypes arise spontaneously, the turquoise killifish has been proposed as a promising model to study spontaneous neurodegenerative processes within the context of aging[3,40].

Here, we investigate whether Aβ plays a role in normal – i.e., non-pathological – brain aging, and whether it can be targeted to mitigate the naturally arising phenotypes of the aging vertebrate brain. Using

transcriptomics, proteomics, and immunohistochemistry, we show that with age, the killifish brain becomes subjected to a robust inflammatory state accompanied by accumulation of pyroglutamated Aβ, a post-translationally modified and particularly toxic Aβ variant[41,42]. Next, we show that age-related brain phenotypes are mitigated by knocking out the *appa* isoform of the Aβ precursor genes.

Results

Amyloid beta is evolutionary conserved between humans and turquoise killifish and is expressed in the aged turquoise killifish brain

Turquoise killifish (strain ZMZ1001) are naturally short lived and reach sexual maturity within 3-5 weeks post hatching. Here, we use as "young", "aged", and "old", killifish from the following ages: 6 weeks, 6 months, and 9 months, respectively (**Figure 1A**). Old individuals display several visually apparent aging phenotypes, including spine curvature, craniofacial alterations, as well as melanocytotic tailfins in males (**Figure 1B**). The brain morphology of the turquoise killifish resembles that of a typical teleost (**Figure 1C**) and has been extensively described elsewhere[43]. The turquoise killifish genome contains two paralogs of the human amyloid precursor protein (APP) which encode the amyloid beta (Aβ) sequence, *appa* and *appb* (coding sequences provided in **Table S1**). Both paralogs show a highly conserved $A\beta_{1-42}$ sequence from human to killifish, as well as conserved beta- and gamma-secretase cleavage sites (**Figure 1D**). Alphafold3 predicts similar 3D architecture for killifish (*appa* derived) and human (*APP* derived) $A\beta_{1-42}$ multimers (**Figure S1A-D**). This becomes evident by the superposition of the C-terminal regions of the isolated monomers (**Figure S1E**). These findings suggest that the high aggregation propensity of $A\beta_{1-42}$ is likely conserved between killifish and humans. To investigate whether Aβ is detectable in the aged turquoise killifish brain, we performed immunohistochemistry using two Aβ-targeting antibodies. Considering that the available antibodies are not specifically raised against the killifish Aβ peptide, together with the known risks of misinterpretation of non-specific signals in the aged brain[44,45], we first addressed the binding specificity of the antibodies. To that end, we used the 4G8 antibody, targeting the $A\beta_{17-24}$ epitope which is fully conserved between humans and killifish, and can bind full-length APP and various APP-derivatives including Aβ. Additionally, we used the pE11 antibody, which targets N-terminally truncated and pyroglutamated Aβ, through recognition of the N-terminal pyroglutamate group and the first six amino acids after truncation ($A\beta_{pE11-16}$) (**Figure 1D**). While 4G8 broadly marks full-length APP and its derivatives, pE11 specifically targets the post-translationally modified Aβ ($A\beta_{pE11}$),

enabling the tracking of cleaved and toxic Aβ rather than its precursors. We focused on detecting $A\beta_{pE11}$, not $A\beta_{pE3}$, as the pE11 target epitope is conserved between humans and killifish. Even though the 4G8 and pE11 antibodies bind different epitopes of the $A\beta_{pE11}$ peptide, we found a strong co-localization between 4G8 and pE11 signal throughout the anterior rhombencephalon (AR) of aged (6-month-old) killifish (**Figure 1E**). To mitigate the possibility that both antibodies bind the same structure in an epitope-independent manner, we blocked the epitopes by incubating antibodies with synthetic $A\beta_{pE11-42}$ peptide prior to the immunohistochemical staining. While incubation with albumin did not impact the staining pattern of pE11 or 4G8, the signal of both antibodies was almost completely abolished by the pre-incubation with $A\beta_{pE11-42}$ peptide, indicating that both antibodies bind to their targets in the killifish brain through their epitope binding domains (**Figure S2A, B**). Taken together, we conclude that the aged turquoise killifish brain contains APP-derivatives including pyroglutamated Aβ.

Turquoise killifish develop age-related brain inflammation while expressing key players of Aβ biogenesis

To investigate the age-dependent expression levels of *appa* and *appb*, as well as other key players of Aβ biogenesis, we performed whole brain RNA-sequencing on six young (6-week-old) and six aged (6-month-old) female turquoise killifish (**Table S2**). Interestingly, genes downregulated with age indicate a strong decline in cellular proliferation (e.g. *mki67*), consistent with the reported loss of neurogenic potential[24,33,34] (**Figure 2A, B**). Genes upregulated with age (e.g., *stat1*, *irf9*, *rsad2*, *cmpk2*) suggest a strong age-related induction of inflammation (**Figure 2C**), which was validated through immunohistochemistry in the hypothalamus and optic tectum targeting Lymphocyte Cytosolic Protein 1 (LCP1), a pan-leukocyte marker previously employed to visualize microglia in the zebrafish and killifish brain[24,34,46] (**Figure 2D-F**). As LCP1 is an actin-binding protein, the staining pattern visualizes the cytoskeletal architecture of microglia instead of their cellular morphology (**Figure S3)**. Next, we investigated the expression of genes from which their human and mice paralogs are key players in Aβ biogenesis as well as close family members, including amyloid precursor proteins *appa*, *appb*, the APP

family members *appl1*, *appl2*, the glutaminyl cyclase *qpctl* which pyroglutamates Aβ, the beta-secretase *bace1* and the family member *bace2* as well as the gamma-secretase subunits *psen1*, *psen2*, *ncstn* and *aph1b*. While all factors showed consistent expression in the turquoise killifish brain, no age-related changes were observed at the mRNA level (**Figure 2G**). In summary, key players involved in Aβ biogenesis are expressed in the turquoise killifish brain, which is subjected to a robust age-related inflammatory state.

$A\beta_{pE11}$ accumulates across the rostro-caudal axis of the killifish brain

Next, we investigated whether the 4G8 and pE11 signals (**Figure 1D, E**) show any age-related changes. In the anterior rhombencephalon (AR) of young 6-week-old fish, 4G8 signal is already easily detectable and covers a similar percentage of the tissue area as seen in their aged 6-month-old counterparts (**Figure 3A-C**), which may reflect the binding of 4G8 to full-length APP. In contrast, the young AR seems largely devoid of any pE11 signal, while pE11 signal was robustly present in the aged AR (**Figure 3D-F**). These findings suggest that while full-length APP and its derivatives might be present in the brain throughout killifish lifespan, $A\beta_{pE11}$ accumulates only at a later age. To explore the full spatiotemporal extent of the accumulation of pyroglutamated Aβ, we characterized the pE11 signal in seven different brain regions along the rostro-caudal axis, at four different ages (**Figure 3G, Figures S4-8**). While pE11 signal remained nearly undetectable until three months of age, the pE11 covered surface area peaked at six months, which was consistent in all investigated brain regions. At nine months of age, the pE11 covered surface area showed a decreasing trend when compared to the six-month timepoint, which suggests an intracellular increase in clearance or a reduced production of $A\beta_{pE11}$. Alternatively, the reduction of pE11 between 6- and 9-months could be due to the death of $pE11^{+}$ cells, or due to the selective disappearance of animals with high $A\beta_{pE11}$ levels. Taken together, these results indicate that $A\beta_{pE11}$ accumulates spontaneously across the rostro-caudal axis between 3- and 6-months of age in the brain of the turquoise killifish.

Amyloid beta predominantly localizes intraneuronally and colocalizes with TUNEL

In the human AD etiology, Aβ is typically known to localize in extracellular beta-sheet aggregates known as Aβ plaques but has also been described to localize intraneuronally[47–52]. To assess Aβ localization in the killifish brain, we first investigated the occurrence of extracellular plaques using the 4G8 and pE11 antibodies. We could not identify any large extracellular signals indicative of the formation of extracellular amyloid plaques. Instead, we found that 4G8 and pE11 signal mainly localized around nuclei, suggesting a predominantly intracellular localization (**Figure 1E**, **Figure S4-8**). To investigate the potential intraneuronal localization of $A\beta_{pE11}$ in the aged killifish brain, we co-labeled pE11 together with an antibody targeting neuronal nuclei (NeuN) and neuronal cytoplasmic marker acetylated tubulin (acTub). Indeed, pE11 localized directly around $NeuN^+$ nuclei (**Figure 4A**) and colocalized with acTub (**Figure S9**), indicating that $A\beta_{pE11}$ predominantly localizes intraneuronally. Pyroglutamated Aβ has been shown to be exceedingly neurotoxic[41]. Therefore, to investigate whether $pE11^+$ cells show signs of DNA double stranded breaks typically indicative of programmed cell death, we adopted TUNEL staining. $TUNEL^+$ cells were nearly undetectable in young killifish brains but were clearly detectable in aged brains (**Figure S10**, **S11**). Importantly, in aged brains TUNEL signal colocalized with pE11 signal (**Figure S12A**), which might suggest that spontaneous accumulation of $A\beta_{pE11}$ could negatively affect neuronal survival in aged killifish. Indeed, $TUNEL^+/NeuN^+$ neurons were detectable throughout the aging killifish rhombencephalon (**Figure S12B**), which is in good accordance with previous literature indicating that the aging killifish brain is subjected to substantial neuronal degeneration and death[29,35–37].

Intraneuronal APP-derivatives aggregate in an age-related manner

Although we could not identify extracellular Aβ plaques, we could detect intracellular $4G8^+$ puncta, suggesting intraneuronal sequestration of APP-derivatives (**Figure 4B**). The $4G8^+$ puncta showed an age-dependent increase in both numbers and covered surface area in the anterior rhombencephalon of the killifish brain (**Figure 4C**, **Figure S13A**). Interestingly, while $A\beta_{pE11}$ is known to be exceedingly aggregation prone[53], most $4G8^+$ puncta were pE11 negative. Although this might indicate that the pE11

antibody is not able to bind its epitope while killifish $A\beta_{pE11}$ is aggregated, the pE11 antibody can detect aggregated human $A\beta_{pE11}$[42,54–56]. Alternatively, the lack of robust pE11 signal in $4G8^+$ puncta might stem from the inaccessibility of aggregated $A\beta_{1-42}$ by dipeptidyl peptidase-4 (DPP4), responsible for the truncation Aβ, a vital step in the formation of pyroglutamated Aβ. Indeed, while AlphaFold protein structure predictions suggest that monomeric killifish (*appa* derived) $A\beta_{1-42}$ can enter the molecular cleft of DPP4 (**Figure S14A**), which holds its catalytic activity[57], this is no longer the case once $A\beta_{1-42}$ has formed multimers (**Figure S14B**). Next, we asked whether the increase in $4G8^+$ puncta could reflect an age-dependent, brain-wide increase in beta-sheet protein aggregation. To this end, we performed a thioflavin-T assay which exploits a change in the fluorescent emission profile of thioflavin-T after its incorporation in beta-sheet aggregates[58]. Aged brain lysates yielded higher thioflavin-T signal compared to their younger counterparts, indicating an age-dependent increase in beta-sheets protein aggregates (**Figure S13B**). The increased abundance of beta-sheet aggregates is consistent with recent literature showing an age-dependent increase of protein aggregation in the killifish brain[28–32]. To directly test the age-dependent aggregation of $4G8^+/pE11^-$ peptides, we performed a filter retardation assay[59]. In short, protein lysates derived from killifish brains of several ages were applied to a filter, which retains protein aggregates of a specific size determined by the pore size of the filter. Next, we stained the filter-bound aggregated protein with either the 4G8 or the pE11 antibody. We found that while $4G8^+$ signal was enriched in an age-dependent manner (**Figure 4D, E**), this was not the case for the detected $pE11^+$ signal (**Figure 4F, G**). Together with the histology data, the results of the filter retardation assay suggest that APP-derivatives, but not $A\beta_{pE11}$, become increasingly aggregated with age in the brain of the turquoise killifish.

CRISPR/Cas9 mediated knock-out of *appa* results in reduction of APP-derivatives

Given the age-dependent accumulation of Aβ, we speculated whether Aβ might contribute to the aging phenotypes of the killifish brain. To test this hypothesis, as well as to investigate whether amyloid precursor protein can be targeted to reduce vertebrate brain aging phenotypes, we generated an *appa*

mutant line using CRISPR/Cas9. Using two guide RNAs targeting the second exon of the *appa* gene, we introduced a 16bp deletion leading to a frameshift. The induced frameshift did not lead to a premature stop-codon but led to an aberrant amino acid coding sequence, which prevented the translation of *appa* derived Aβ peptide. In addition to *appa*, we also targeted its homologue, *appb*, for knock-out. While successfully inserting mutations in the *appb* gene, founders could not be raised to adulthood and were therefore excluded from analysis. The loss of *appb* mutant carriers might indicate a role for *appb* in killifish development, which is in line with the described role for *appb* during early zebrafish development[60]. To investigate whether *appb* acts redundantly to counteract the lack of *appa*-derived APP, we performed a Western blot using the 22C11 antibody targeting the full-length APP. 22C11 should target both wild-type APPA and APPB, as the epitope targeted by 22C11 is highly conserved in both homologues (16/16 amino acids) and might also detect killifish APLP2 (12/16). APLP1 is less conserved (9/16). We observed a significant reduction (>50%) of APP levels in the killifish *appa* mutant brain lysates, indicating that the still functional *appb* could not compensate in full for the loss of *appa* derived APP (**Figure 5B, C**). At 6-months of age, the reduced levels of APP led to a reduction in APP-derivatives, including $A\beta_{pE11}$, indicated by the observed reduction in 4G8 and pE11 signal intensity as well as a reduction in the surface area covered (**Figure S15, Figure 5D, E**). The reduced immunoreactivity for both antibodies in the *appa* mutants further supports their binding specificity to peptides derived from the gene encoding for amyloid precursor protein a. Residual antibody immunoreactivity likely stemmed from *appb* derived Aβ. In contrast to the total signal intensity and covered surface area of 4G8 and pE11, the surface area covered by $4G8^{+}$ puncta remained unchanged compared to wild-type siblings in the 6-months old *appa* mutant hypothalamus superior lobe and anterior rhombencephalon (**Figure S16A**), suggesting that while non-aggregated $A\beta_{pE11}$ is decreased in *appa* mutant brains, the quantity of aggregated APP derivatives remained stable.

Brain aging can be mitigated through *appa* knock-out, evading cellular death and inflammation

To investigate the effects of the knock-out of *appa* in an unbiased manner, we performed liquid chromatography mass spectrometry (LC-MS) on whole brain lysates (**Table S3**). We used three males and three females from both *appa* mutants, as well their wild-type siblings, for each of the two age groups (6- and 7.5-month-old). The time-point of 7.5 months was chosen as it corresponds to the median lifespan of fish from the ZMZ1001 strain (**Figure 1A**), at which behavioral changes become apparent[37,39]. At both timepoints, a strong reduction in *appa* derived peptides (APPA) was found in the *appa* mutants, while *appb* derived peptides (APPB) showed no significant changes (**Figure 5F-I**). The LC-MS data support the notion that the *appa* mutants are full APPA knockouts, considering that the residual APPA signal likely stems from the miss-mapping of a single peptide derived from *appb* (89% sequence similarity), which is further compounded by the imputation strategy employed to deal with missing values of lowly abundant peptides in biological replicates. At 6-months of age, the *appa* mutants displayed an upregulation of proteins involved in mitochondria (e.g. DHRS12, SLC25A3, NDUFV1), translation (e.g. RPS7, RPL27, RPS13), and DNAJ-chaperones (e.g. DNAJC5AA, DNAJA1L, DNAJB3, DNAJA3A), as well as a downregulation of amyloidosis associated factors Apolipoprotein A1 (APOA1) and beta-synuclein (SNCB) (**Figure 5F, G**). Compared to same-aged wild-type siblings, 7.5-month-old *appa* mutants showed an upregulation of keratins (e.g. KRT4, KRT5, KRT18) and a downregulation of proteins involved in the lysosome and proteasome, as well as proteins involved in inflammation related ontologies such as the defense response (e.g. C4B, TGFB1) and the JAK-STAT cascade (e.g. STAT1A). In addition, we observed a downregulation of proteins involved in necroptosis (e.g. MLKL, XIAP) which is suggestive of a reduction in programmed cell death (**Figure 5H, I**). To validate the potential mitigation of age-related cell death in the *appa* mutants, TUNEL staining was performed in tissue sections of the hypothalamus superior lobe and anterior rhombencephalon. While TUNEL$^+$ cells were consistently present in brains of wild-type sibling, *appa* mutant brains contained a lower TUNEL$^+$ covered surface area in both investigated regions at as early as 6-months of age (**Figure 5J-L**). In addition, staining for (pro)caspase3, which marks (pre-)apoptotic cells[61], showed a similar decrease in 6-months-old *appa* mutants (**Figure S16B**). To validate the potential mitigation of age-related inflammation, we performed

an immunohistochemical staining using an antibody targeting Lymphocyte Cytosolic Protein 1 (LCP1), an actin-binding pan-leukocyte marker previously used to visualize microglia in the killifish and zebrafish brain[24,34,46]. The 6-months-old *appa* mutant brain displayed a significant reduction of LCP1 covered surface area in the hypothalamus superior lobe, and a declining trend in the anterior rhombencephalon (**Figure 5M-O**). Taken together, the LC-MS and histology results indicate that the knock-out of *appa* mitigated spontaneous cell death and inflammation in the aging turquoise killifish brain. To determine whether the beneficial effects of *appa* knock-out are restricted to inflammation and cell death, or whether they represent a broader mitigation of brain aging, we conducted a proteome-wide analysis. Protein group abundances were compared between young (6-week-old) and aged (6-month-old) brains, as well as between *appa* mutant and wild-type sibling brains at two different ages (6 and 7.5 months). Subsequently, the log2 fold-change (log2FC) values from both the young-versus-old and appa mutant-versus-wild-type comparisons were plotted against one another. In 6-month-old *appa* mutants, the differentially abundant proteins did not correlate with age-related changes in protein level (**Figure 5P**). However, in 7.5-month-old *appa* mutants, we observed a strong negative correlation (slope = -0.265, p = 2.31e-13) indicating that proteins upregulated with age were downregulated in the mutants, and *vice versa* (**Figure 5Q**). Proteins upregulated with age but downregulated in the *appa* mutants included proteins implicated in neurodegenerative diseases (e.g. APOEB, PFN1, LGALS9) and inflammation (e.g. IFI44L, C4B, CMPK2), while proteins downregulated with age and upregulated in the *appa* mutants included extracellular matrix components (e.g. COL1A2, KRT5) as well as proteins involved in neuronal function (e.g. GRM8, PCDH2AC, PPFIA2). These findings indicate that *appa* knock-out mitigated brain aging in a proteome-wide manner, extending beyond the reduction of inflammation and cell death.

Knock-out of *appa* mitigates age-related learning decline

Turquoise killifish display a spontaneously occurring decline in learning capacity with age, a *bona fide* measure of age-related cognitive decline[37,39]. To investigate whether APP/Aβ contributes to non-pathological age-dependent learning deficiency, we developed an active avoidance test based on previous

literature[37,62,63]. In short, fish (28 *appa* mutants and 30 wild-type siblings) were individually tested by placing them in an arena consisting of two circular compartments, connected through a narrow opening (**Figure 6A**). After a 15-minute acclimatization period, fish were subjected to 40 consecutive cycles, where a conditionate stimulus (light), was coupled with a non-conditioned stimulus (air bubbles). Each one-minute cycle corresponded to 30 seconds of light exposure, with the latter 15 seconds combined with exposure to air bubbles, followed by a rest phase of 30 seconds. Untrained fish showed a preference to remain in the light, with 84% of the fish staying within the light during the first cycle of the experiment (**Figure 6B**). Due to the pairing of the light with an adverse non-conditioned stimulus (air bubbles) across the 40 cycles, the fish learn to avoid air bubbles once cued with light. Indeed, even 7.5-month-old wild-type fish (n = 30) become increasingly proficient at actively avoiding the light with 16% (first cycle) to 46% (last cycle) of the fish escaping the bubbles (**Figure 6B**, **Figure S17, Table S4**). However, the 7.5-month-old *appa* mutants (n = 28) outperform their age-matched wild-type siblings and show an increased rate of successful escapes after the 6th cycle onwards, while reaching an average escape rate of 55% during the last cycle (**Figure 6B**, **C**, **Figure S17**). Comparing the total amount of successes, as well as their top scores, defined as the maximum number of successes in a 10-cycle window, show higher learning performance in the *appa* -/- mutants ($p = 0.073$ and $p = 0.265$, respectively) (**Figure 6C**, **D**). Significant improvements in the *appa* -/- mutants were observed when comparing the speed at which their top scores were reached (**Figure 6E**) and when considering both top scores and the speed at which the top score was reached simultaneously (**Figure 6F**). To gain insight into the biological significance of the learning improvements observed in the *appa* -/- mutants at 7.5-months of age, we performed the active avoidance test on an independent cohort of young killifish (6-week-old, n = 16) (**Figure S18**). While young fish show a higher escape rate in the first 5 cycles of the experiment compared to all other non-young counterparts, the 7.5-month-old mutants performed not only better than age-matched controls, but similar to young fish for the remaining cycles. These results suggest that knock-out of *appa* can almost completely rescue the age-related learning deficit observed in turquoise killifish. Newly learned behaviors (e.g. the negative association with red light) are encoded within a neuronal network which, upon

activation, expresses the immediate response factor c-Fos[64,65]. To address whether the active avoidance test we employed led to the activation of such a network, and whether the *appa* mutants show increased network activity compared to their wild-type siblings, we used hybridizing chain reaction (HCR) *in situ* hybridization. We used HCR to visualize *fos* transcripts in brains isolated immediately after the 40th cycle of the active avoidance task (**Figure 6G-J**). We specifically quantified the percentage surface area covered by *fos* transcripts in the medial zone of the telencephalon (**Figure 6K**), considering that this region has been previous implicated in learning performance of other fish species[66]. Importantly, the *appa* mutants that underwent the active avoidance test showed higher *fos* levels in the medial zone when compared to untested fish, as well as their wild-type siblings that did undergo the active avoidance test (**Figure 6L**). From these results, we conclude that *appa* knock-out resulted in the enhanced establishment of a learning-induced neuronal network, as well as the rescue of an age-induced learning deficit observed in turquoise killifish.

Discussion

In this study, we asked whether the detrimental effect of Aβ on the brain is limited to neurodegenerative diseases, or whether Aβ also impacts normal, non-pathological brain aging. Although Aβ has been shown to accumulate during normal aging, convincing experimental proof of its causal effect remained absent. An important clue suggesting a potential causal effect of Aβ in the normal aging brain was provided by a previous study describing the cognitive fitness of aged human carriers of the Islandic APP variant (A673T). The A673T APP mutation leads to a reduction in β-Secretase 1 (BACE1)-mediated Aβ production[67], which not only correlated with a reduced risk to develop Alzheimer's disease (AD), but also with increased cognitive fitness in healthy aging individuals[68]. Here, we provide the first experimental evidence showing that lowering Aβ levels in wild-type vertebrates can reduce brain aging phenotypes and mitigate age-related cognitive decline.

Aβ is attributed to drive protein aggregation, inflammation, and neurodegeneration within the context of AD, leading to cognitive decline. However, while current endeavors lowering extracellular Aβ plaques in patients with early AD can significantly slow down cognitive deterioration, the effect size remains marginal[14]. Together with the observation that Aβ accumulation is not restricted to AD patients but is also observed in normal aging individuals, the formerly widely accepted central role of Aβ in AD is now a matter of intense debate. Here, we show that the negative effect of Aβ on brain function is not limited to AD but instead could have a much broader effect as a contributor of normal brain aging.

To investigate the effect of Aβ during normal brain aging, we have employed the turquoise killifish. These annual teleosts have developed a compressed lifespan due to the relaxed purifying selection of deleterious mutations acting in late life[69]. Therefore, the turquoise killifish genome carries an exceptionally high mutation load, which likely forms the polygenic basis of their robust aging phenotypes and compressed lifespan. Due to their short lifespan, turquoise killifish form an ideal model for functional studies investigating vertebrate aging. In this study, we recapitulate previously reported brain aging phenotypes of the turquoise killifish, including the aggregation of protein, inflammation, and cellular degeneration. Furthermore, we describe an additional brain aging phenotype, the intraneuronal

accumulation of $A\beta_{pE11}$. In human AD brains, intraneuronal $A\beta_{pE11}$ has been described[56]. However, whether this is also observed in aged non-diseased brains remained to be investigated. In addition, while $A\beta_{pE3}$ is expressed and studied in AD mouse models (e.g. 5xFAD)[70], no animal data are available yet for the expression of $A\beta_{pE11}$. Therefore, our finding that turquoise killifish accumulate intraneuronal $A\beta_{pE11}$ in an age-related and spontaneous manner, enables the possibility to use this emerging animal model to study the effects of $A\beta_{pE11}$ within the context of natural aging.

While pE11 signal did not show robust signs of aggregation, intracellular $4G8^+/pE11^-$ puncta accumulated throughout the aging killifish brain. Filter retardation assays confirmed that $4G8^+$ protein aggregates accumulate in aging killifish brains and this is not the case for $pE11^+$ aggregates. Although we cannot exclude the possibility that the target epitope of the pE11 antibody is not accessible while $A\beta_{pE11}$ is in an aggregated state in the killifish brain, this option is unlikely considering that the pE11 antibody is able to bind aggregated $A\beta_{pE11}$ in human brains[42,54–56]. Another hypothesis which could help to explain the different aggregation dynamics of $pE11^+$ and $4G8^+$ peptides could be that pyroglutamation of Aβ might prevent its aggregation. However, pyroglutamation of Aβ is known to increase its aggregation propensity *in vitro*[53], hence one would not expect the opposite effect *in vivo*. Instead, we postulate that the aggregation of Aβ might prevent the formation of $A\beta_{pE11}$, which is supported by our Alphafold modeling showing that multimeric Aβ can no longer enter the molecular cleft of DPP4, a vital step in the formation of $A\beta_{pE11}$. This exciting possibility would be in line with a previously proposed theory in which the sequestering of Aβ could prevent the formation of highly toxic Aβ derivatives, which would therefore have a protective effect in the short term[71].

To test the effect of Aβ during normal aging, we knocked out one the amyloid precursor protein coding genes, *appa*. The results obtained through LC-MS suggested that *appa* knock-out mitigated cellular death and inflammation in aged killifish brains, which we validated through a histological approach. Furthermore, proteome-wide analysis indicated that the beneficial effects of *appa* knock-out are not restricted to inflammation and cell death but encompass a much broader, proteome-wide mitigation of brain aging. The beneficial effects of *appa* knock-out on brain aging in the turquoise killifish is in stark

contrast with the negative effects observed in APP knock-out mice, which are viable but have altered neurogenesis and smaller brains[72]. Aged APP knock-out mice display increased reactive gliosis in the neocortex and hippocampus and show reduced locomotor activity[73], as well as reduced memory retention[74]. It has been suggested that both, excessive amounts of Aβ, as well as complete depletion of Aβ, has negative effects on brain functionality[75]. As teleosts, turquoise killifish have been subjected to a whole genome duplication[76] and hence, contain two APP paralogues. Therefore, while knockout of APP in mice resulted in a complete depletion of Aβ, knock-out of *appa* in killifish left the fish with *appb*, which might have yielded a concentration of Aβ high enough to allow typical brain development and function, but low enough to evade Aβ-mediated exacerbation of brain aging phenotypes.

To investigate whether Aβ exacerbates cognitive decline in aged killifish, we performed an active avoidance test on the *appa* mutants and their siblings. Excitingly, we found that the *appa* mutants outperform their wild-type siblings, reaching a learning performance like that observed in an unrelated cohort of young killifish. The improved learning capacity observed in the *appa* mutants was further supported by increased levels of *fos* transcripts in the medial zone of the telencephalon, known to harbor neurons involved in operant conditioning [66]. In sum, we conclude that the knock-out of *appa* in the turquoise killifish could rescue a substantial part of their age-related learning deficit.

While decades of research have focused on elucidating the effect of Aβ during Alzheimer's disease, the effects of Aβ accumulation during normal aging remained largely unexplored. Here, we show that the detrimental effects of Aβ on brain health are not limited to a specific pathology but instead broadly effect the aging brain.

Methods

Fish husbandry and maintenance

The turquoise killifish (ZMZ1001 strain) were housed in individual 2.8L tanks equipped with baffles, fry mesh and lids glass capillaries (Aquaneering, USA) connected to a system with circulating water. Fish received 12 h of light and 12 h of darkness per day. Water temperature was set to 28°C. Fish were fed with brine shrimp nauplii (*Artemia salina*) and blood worm larvae (*Chironomus spp.*) twice a day during the week and once a day during the weekend. Adult fish (6 weeks post hatching) were used for breeding purposes. One male and up to three females were housed in 9.5L breeding tanks equipped with baffles, fry mesh and lids glass capillaries (Aquaneering, USA). Fertilised eggs were regularly collected using sand boxes and then stored in a petridish with coconut fiber at 24°C. Three weeks prior to hatching, embryos were placed at 28°C. Furthermore, the husbandry and maintenance of the killifish used in this study were performed as part of the standard operating procedure the Leibniz institute on Aging, which was described in detail in a previous publication[77]. The experiments were carried out under permission of the following animal experimental licenses: FLI-21-016 (young behavioral tests), FLI-23-029 (appa KO versus wild-type behavioral tests), Par.11 J-003798 (Maintenance and Housing), FLI-22-203 (Genotyping), O-DV-23-27 (Organ harvest license).

Protein alignment and Alphafold protein structure predictions

To determine how similar protein sequences of APPA and APPB from turquoise killifish are to protein sequences from humans (*H. sapiens*), mice (*M. musculus*) and zebrafish (*Danio rerio*), full-length peptide sequences were aligned using UniPro UGENE (RRID:SCR_005579). Multiple protein sequences were aligned with the MUSCLE default mode. The sequences of all protein variants from online database Ensembl (https://www.ensembl.org/index.html). Structure predictions of $A\beta_{1-42}$ and its complex with DPP4 were performed using the AlphaFold3 web server with default options[78]. For graphical representations the program ChimeraX[79] was employed.

Brain processing for cryo-sectioning

Killifish were euthanized using rapid-chilling method. The whole head was first fixed in 4% paraformaldehyde overnight at room temperature. The next day brain was isolated, washed in 4% sucrose and incubated in 30% sucrose overnight at 4°C. On the last day, brain was transferred to an appropriate Tissue-Tek cryomold, immersed in the Tissue-Tek O.C.T. Compound and transferred to the dry ice to quickly freeze the tissue. Brains were stored at -80°C until the sectioning step. The tissue blocks were sectioned to 10 µm thin sections using cryostat machine, while following standard protocol for cryo-sectioning.

Immunohistochemistry

Thawed slides were first washed in PEMTx solution (80 mM 98.5+% PIPES (1,4-Piperazin-bis-(ethansulfonacid), 5 mM EGTA, 1 mM $MgCl_2$, 0.2% Triton X-100 in milliQ water, pH 7,5) for 10 min, in NH_4Cl-PEMTx (50 mM of NH_4Cl in PEMTx) for another 10 min, and then two more times in PEMTx. The slides were transferred and incubated in Sodium Citrate Solution (10 mM 99% Trisodium Citrate Dihydrate in RO H_2O, pH 6) for 15 min at 85°C in the waterbath. Once cooled down to the room temperature, slides were washed two times for 10 min in PEMTx. The tissue was incubated in the blocking solution (10% Fetal Bovine Serum, 1% DMSO in PEMTx) for 1 hour at room temperature in a humidified chamber. Slides were later incubated with primary antibodies diluted in a blocking buffer at 4°C overnight in a humidified chamber. The following day, the slides were washed in PEMTx solution five times for 20 min (on a shaker). The slides were incubated in the secondary antibody (1:500) and DAPI (1:1000) diluted in a blocking buffer for 1 h at room temperature in a humidified chamber and in the dark. The primary antibody Rabbit Anti-Abeta-pE11 was combined with the secondary antibody Alexa Fluor® 647 Donkey anti-rabbit IgG (min. x-reactivity) antibody (BioLegend, USA, Cat# 406414, RRID: AB_2563202). The Rabbit Anti-GFAP antibody was combined with the secondary antibody Alexa Fluor 555 (Thermo Fisher Scientific, USA, Cat# A-21428, RRID: AB_2535849). The slides were washed

in PEMTx solution five times for 10 min, then two times for 7 min in PEM solution (80 mM 98.5+% PIPES (1,4-Piperazin-bis-(ethansulfonacid), 5 mM EGTA, 1 mM $MgCl_2$ in miliQ H_2O) on the shaker and in the dark. Slides were mounted in the ProLong Gold antifade reagent and stored at 4°C in the dark. The slides were imaged using Zeiss Axio Scan.Z1 microscope with a Plan-Apochromat 20x/0.8 M27 objective, Axiocam 506m imaging device and 1x Camera Adapter. Different imaging settings were used for different stainings. For all types of staining the effective numerical aperture was 0.8 and the binning mode 1.1. Imaging results were processed using ZEN 3.5 (Blue Edition) ZEN Digital Imaging for Light Microscopy (RRID:SCR_013672) to select images and Fiji (ImageJ2, RRID:SCR_002285) and Imaris (V10.2, 2024 June 26) to quantify positive signal.

Used antibodies:

Antibody	**Used for**	**Dilution**	**Ordering details**
Rabbit polyclonal purified Anti-Abeta-pE11	IHC	1:200	Synaptic Systems, AB_2619913
Mouse anti APP A4 clone 22C11	WB	1:5000	Millipore, MAB348
anti-mouse IgG HRP conjugate	WB	1:10000	Promega, W402B
Anti-Acetylated Tubulin, Mouse Monoclonal (Clone 6- 11B- 1)	IHC	1:100	Sigma-Aldrich, T7451
Anti-β-Amyloid, 17-24 Antibody (4G8), mouse monoclonal	IHC	1:100	Biolegend, SIG-39200
Anti-LCP1, rabbit polyclonal	IHC	1:100	GeneTex, GTX124420
Anti-NeuN, mouse monoclonal (clone A60)	IHC	1:150	Sigma-Aldrich, MAB377
Anti-Caspase-3 (31A1067), mouse monoclonal	IHC	1:100	Novus, NB100-56708SS
Anti-rabbit Alexa555 (IgG, H+L)	IHC	1:500	Invitrogen, A21428
Anti-rabbit Alexa647 (IgG, H+L)	IHC	1:500	Invitrogen, A27040
Anti-mouse Alexa555 (IgG, H+L)	IHC	1:500	Invitrogen, AB_2535844
Anti-mouse Alexa647 (IgG, H+L)	IHC	1:500	Invitrogen, A21235
Anti-rabbit-HRP	FRA	1:5000	Dianova
anti-mouse-HRP	FRA	1:2000	Sigma-Aldrich

RNA sequencing

Brain dissection was followed by RNA isolation using the TRIzol reagent (Life Technologies, Carlsbad, CA, USA) according to the manufacturer's instructions. RNA integrity and concentration were measured using Agilent 4200 TapeStation System in combination with RNA ScreenTape (Agilent Technologies, Santa Clara, CA, US) ensuring high quality RNA (RNA Integrity Numbers > 8) for library preparation. Libraries for Illumina next-generation sequencing technology[80] were prepared from 200 ng of total RNA using NEBNext Ultra II Directional RNA Library Preparation Kit in combination with NEBNext Poly(A) mRNA Magnetic Isolation Module and NEBNext Multiplex Oligos for Illumina (Unique Dual Index UMI Adaptors RNA) following the manufacturer's instructions (New England Biolabs, Ipswich, MA, US). Library quantification and quality assessment were performed using Agilent 4200 TapeStation System with D5000 ScreenTape. Libraries were then pooled and sequenced on NovaSeq 6000 platform (Illumina, San Diego, CA, US) using the SP 100 cycle v1.5 kit with a 51-cycle paired-end read configuration. A minimum sequencing depth of 33.2 million reads per sample was achieved. Sequencing data were converted to FASTQ format using bcl2fastq (v2.20.0.422).

RNA sequencing data analysis

Raw sequencing data (FASTQ files) were evaluated for quality using FastQC (v0.11.9). Adapter sequences, poly-A sequence and low-quality bases were removed using cutadapt (v4.2). High-quality reads were aligned to the reference genome (*Nothobranchius furzeri*, MPIA_NFZ_2.0) using STAR (2.7.6a) and PCR duplicates were removed based on unique molecular identifiers by umi-tools (1.1.1, parameter: --chimeric-pairs discard --unpaired-reads discard –paired). Gene-level quantification was performed using featureCounts (v2.0.3, parameter: -s 2 -p -B --countReadPairs) based on annotated gene features (obtained through personal communication with David Willemsen, corresponding to[81]. Differentially expressed genes were obtained using the R package EdgeR[82] and gene ontologies were obtained using the online tool DAVID[83].

TUNEL staining

To visualize apoptotic cells in the killifish brain, cryosections (fixed in 4% PFA, sectioned 10um thick) were stained using the In Situ Cell Death Detection Kit, TMR rot (12156792910) from Roche. In short, cryosections were air dried for 15 seconds, and washed in PBS + 0,2% Triton-X100 for 3 times 10 minutes. Three washes in PBS, of each 5 minutes, were followed by placing the slides in a humidified box, and the brain sections of interest were encircled by a hydrophobic pen. Next, TUNEL staining solution was added on top of the sections which were placed, inside of the humidified box, in a 37°C incubator for 60 minutes. Afterwards, the slides were washed 3 times for 5 minutes in PBS and incubated with PBS+ DAPI (1:000 dilution) for 20 minutes in the humidified box. Last, the slides were washed 3 times for 5 minutes with PBS and mounted using Prolong Gold. Imaging and quantification were performed as described for immunohistochemistry, utilizing TUNELs excitation spectrum at 540nm and a emission spectrum between 570-620nm.

Western blot analysis

Liquid frozen brains of killifish appa -/- and age matched controls of 6-months of age were lysed in 300µls 4xLämmli sample buffer (4 ml 20% SDS, 4 ml glycerol, 1ml ß-mercaptoethanol, 1 pinch bromophenol blue, 1,25 ml 1M Tris pH 7,6) using a tissue homogenizer. After boiling for 10 min at 95°C while shaking at 600 rpm, the samples were centrifuged 1 min at 11000 rpm. 20µls of the total lysate were loaded on Schägger gels. After 60 mins transfer to nitrocellulose blotting membrane (0,1 µm, Amersham™ Protran, product 10600005) at 400 mA, the membrane was boiled for 5 mins in 1 x PBS, then incubated in 1 x PBS for 30 mins at room temperature before blocking with 0,2% Tropix I-Block (Applied Biosystems) for 1 hr at room temperature on a rotating platform. The incubation in primary antibody 22C11 (Mouse anti APP A4 clone 22C11, Millipore MAB348, 1:5000 in I-Block) was done overnight at 4°C. After removal of the primary antibody, the membrane was washed 4 x 15 mins in I-Block, followed by 1 hr incubation in a 1:10000 dilution of the secondary antibody (anti-mouse IgG HRP conjugate, W402B, Promega) at room temperature. The membrane was washed 4 times 15 mins and 3

times 10 mins with 1 x PBS before detection of bound antibodies with ECL plus (Pierce ECL Plus Western Blotting substrate, Thermo Scientific). After images were acquired using the LAS-4000 image reader (Fujifilm Life Science), the membrane was washed 4 x 15min in PBST, blocked in 3%milk for 1hr at room temperature and then incubated with the primary anti-□-tubulin antibody T6199 (Sigma) 1:100 000 in I-Block overnight at 4°C. After removal of the anti-a-tubulin antibody antibody, the membrane was washed 4 x 15 min in I-Block, followed by 1 hr incubation in a 1:10000 dilution of the secondary antibody (anti-mouse IgG HRP conjugate, W402B, Promega) at room temperature. The membrane was washed 4 x 15 min and 3 x 10 min with 1 x PBS before detection of bound antibodies with ECL plus (Pierce ECL Plus Western Blotting substrate, Thermo Scientific). Images of 22C11 and □-tubulin were quantified with the software ImageJ. For each group biological triplicates were quantified.

Filter retardation assay

Brain tissues were transferred to 2 mL Precellys tubes containing a mix of 1.4 mm and 2.8 mm ceramic (zirconium oxide) beads, in 200 µL of BPS-PIS buffer. Two cycles of mechanical homogenization were carried out at 6000 rpm for 30 seconds each, with a 30-second break on ice between each cycle, using the Precellys 24 lysis and homogenizer (Bertin, France). Subsequently, the tubes were centrifuged at 3000 rpm for 5 min at 4°C. The resulting supernatant was carefully transferred to a new 1.5 mL low-binding tube. An equal volume of 2X lysis buffer was added to the homogenate and sonicated (Bioruptor Plus, Diagenode, Belgium) for 20 cycles (60 sec ON/30 sec OFF) at 4°C. The protein concentration in the lysate was quantified using the Pierce™ BCA Protein Assay Kit (Thermo Fisher Scientific, Cat. no. 23227). For the filter retardation analysis, we adapted a previously published protocol[59]. In brief, 100 µg of protein was loaded in duplicate onto a 0.2 µm cellulose acetate membrane (Cytiva, Cat. no. 10404180) that had been pre-equilibrated in 1X TBS. The membrane was washed twice with a wash buffer (150 mM NaCl and 10 mM Tris, pH 8.0), then blocked with 5% milk. This was followed by incubation with primary antibodies: Rabbit-anti-pE11 (1:500, Synaptic Systems) or Mouse-anti-4G8 (1:1000, BioLegend), overnight. Subsequent incubation with secondary antibodies was performed using anti-

rabbit-HRP (1:5000, Dianova) and anti-mouse-HRP (1:2000, Sigma-Aldrich) for 4 h. The images were captured in Amersham imager 600, and quantification was performed using Fiji ImageJ software. Buffers: BPS-PIS: 250 µL PBS; 5 µL Protease inhibitor cocktail; 25 µL PhosSTOP. Lysis Buffer (2X): 225 µL PBS; 25 µL SDS (10%); 12.5 µL HEPES (2M). Tris-buffered saline (TBS) 10X, pH 8: 200 mM Tris base; 1.5 M NaCl. Tris-buffered saline with Tween (TBS-T): 1X TBS; 0.1% Tween 20.

Thioflavin-T assay

Whole brain protein lysates were produced using the same protocol as described to LC-MS. Black and transparent bottom 96-well plate (Greiner 96 F-bottom, Thermo Fisher #165305) were used, as well as the CLARIOstar Plus (BMG Labtech) plate reader. Thioflavin-T powder was bought from Sigma-Aldrich (T3516). To produce the Thioflavin-T (ThT) working solution, 80mg of ThT-powder was added to 25mL of dPBS (Gibco, [-] Cacl [-] MgCl) to make a 10mM stock. The solution was vortexed and incubated for 1 hour at room temperature. After the almost complete dissolvement of the ThT, 10mL of the ThT solution was filtered through a 0.2µm filter using a syringe. Next, 200µl of the filtered ThT solution was added to 1700µl of dPBS, to make the working solution of 50µM, and kept in the dark until further use. Next, protein lysates (49µl of 1.325µg/µl) was added to the 96-well plate (F-bottom). Using a multichannel pipet, 1µl of the ThT working solution (50µM) was added to the wells, and the plate was entered in the plate reader directly. The following imaging settings were used: Microplate: Greiner 96 F-bottom; Presets: CFP; Exitation: 430-20nm; Dichroic: auto 455nm; Emission: 480-20nm; Well scan: none; Optic: Bottom optic; Settling time: 0.2; Flying mode: off; No. of kinetic windows: 1; No. of cycles: 10; No. of flashes: 50; Cycle time: 60; Shake: Before first cycle; double orbital, 100rpm, 10sec. Values were recorded after 3 minutes and 30 seconds. Biological replicates were used in duplo, and averaged values were plotted.

CRISPR/Cas9 transgenesis

CRISPR/Cas9 tool was used to edit the genome of the turquoise killifish. Guide RNA templates were designed using an online program CHOPCHOP (https://chopchop.cbu.uib.no/). Exon 2 of *appa* was targeted using two different gRNAs, and Exon 3 of *appb* was targeted using three different gRNAs. Templates of ssDNA target-specific oligonucleotides were used for sgRNA synthesis. Used guide RNA's (regions in bold indicate the complement sequence of the target):

***appa* sgRNA1**	TAATACGACTCACTATAGG**TCAACGTTCAGAGCGGCAAG**GTTTTAGAGCTAGAAATA GCA
***appa* sgRNA2**	TAATACGACTCACTATAGG**CAAGTGGGAGTCCGACCCCT**GTTTTAGAGCTAGAAATAGCA
***appb* sgRNA 1**	TAATACGACTCACTATAGG**AAACCCACCGAGTCATCCAAAG**GTTTTAGAGCTAGAAATAGCA
***appb* sgRNA 2**	TAATACGACTCACTATAGG**ACAGATCACGAATGTCGTAG**GTTTTAGAGCTAGAAATAGCA
***appb* sgRNA 3**	TAATACGACTCACTATAGG**CATTCGTGATCTGTAGCTCT**GTTTTAGAGCTAGAAATAGCA

The template ssDNA target-specific oligonucleotide to synthesise gRNA was designed by adding an overlapping nucleotide sequence to the N-terminus and T7 promoter sequence to the C- terminus. The PAM sequence (NGG) was removed from the sequence. Templates were synthesised and delivered by the Integrated DNA Technologies (https://eu.idtdna.com/pages/products/custom-dna-rna/dna-oligos). The sgRNAs were synthetised using the EnGen® sgRNA Synthesis Kit (New England BioLabs, USA, #E3322V), according to their standardized protocol. The synthesised sgRNAs was cleaned up with the Monarch® RNA Cleanup Kit (50µg, New England BioLabs, USA, #T2040L), following the instructions. For CRISPR/Cas9 injections, concentration of sgRNA solution was adjusted to 300 ng/µL. The CRISPR/Cas9 and gRNA reaction mix was prepared with EnGen® Spy Cas9 NLS (20 µM, New England Biolags, USA), by mixing 1 µL of Cas9 NLS, 1 µL of each purified sgRNA (300 ng/µL), 2 µL Phenol Red for visualisation and nuclease free water up to 10 µL (kept on ice). The needles were pulled from glass capillaries 1.0 OD x 0.58 ID x 100 L mm using a micropipette puller machine with the program previously established in the lab. One- or two-cell stage embryos were placed and fixed in the agarose plate and injected with a small amount of reaction mix directly into the embryos one at a time. The embryos were transferred to the clean methylene blue solution, checked daily and further handled as previously described for embryo maintenance. To genotype CRISPR/Cas9 injected fish and their progeny,

first fish DNA had to isolated from 2-4 scales which were collected from the posterior part of the body of sexually matured fish (minimum 5-6 weeks of age). The scales were transferred to 50 µL of SEL buffer (1M KCl, 1M $MgCl_2$, 1M Tris pH 8,3, 10% Igepal, 10% Tween-20, 0,1% Gelatine in miliQ H_2O) and 1 µL of Proteinase K. The scales were incubated in the SEL isolation buffer and Proteinase K at 60°C for 1 h, 90°C for 15 min and 12°C until tubes were taken out of the machine. The isolated DNA was used as a template for PCR amplification of the target region of interest. *Taq* 2X Master Mix was used for the PCR reaction. PCR details. Forward primer: CCTCTCTTTCAGGTCCCCAC. Reverse primer: TTTTCTGCTCTGCT TTTAGGC. Amplicon Length: 209 bp. CONDITIONS: **(1x)** 3:00 95.0C **(35x)** 0:45 95.0C 0:30 55.0C 0:45 72.0C **(1x)** 5:00 68.0 ∞ 10.0 PCR amplicons were purified using Sera-Mag SpeedBead Carboxylate-Modified Magnetic Particles (Hydrophylic) magnetic beads. Purified DNA was sent for Sanger sequencing to the Eurofins Genomics (https://eurofinsgenomics.eu/).

Sample preparation for proteomics analysis

Before lysis, lysis buffer (fc 4% SDS, 100 mM HEPES, pH 8.5, 50 mM DTT) was added to each samples. Samples were then boiled at 95°C for 7 min and sonicated using a tweeter. Reduction was followed by alkylation with 200 mM iodoacetamide (IAA, final concentration 15 mM) for 30 min at room temperature in the dark. Samples were acidified with phosphoric acid (final concentration 2.5%), and seven times the sample volume of S-trap binding buffer was added (100 mM TEAB, 90% methanol). Samples were bound on 96-well S-trap micro plate (Protifi) and washed three times with binding buffer. Trypsin in 50 mM TEAB pH 8.5 was added to the samples (1 µg per sample) and incubated for 1 h at 47°C. The samples were eluted in three steps with 50 mM TEAB pH 8.5, elution buffer 1 (0.2% formic acid in water) and elution buffer 2 (50% acetonitrile and 0.2% formic acid). The eluates were dried using a speed vacuum centrifuge (Eppendorf Concentrator Plus, Eppendorf AG, Germany) and stored at -20° C. The samples were loaded on Evotips (Evosep) according to the manufacturer's instructions. In short, Evotips were first washed with Evosep buffer B (acetonitrile, 0.1% formic acid), conditioned with 100% isopropanol and equilibrated with

Evosep buffer A. Afterwards, the samples were loaded on the Evotips and washed with Evosep buffer A. The loaded Evotips were topped up with buffer A and stored until the measurement.

LC-MS Data independent analysis (DIA)

Peptides were separated using the Evosep One system (Evosep, Odense, Denmark) equipped either with a 15 cm x 150 µm i.d. packed with a 3 µm Reprosil-Pur C18 bead column (Evosep Endurance, EV-1109, PepSep, Marslev, Denmark) or with a a 15 cm x 150 µm i.d. packed with a 1.5 µm Reprosil-Pur C18 bead column (Evosep Performance, EV-1137, PepSep, Marslev, Denmark) heated at 45°C with a butterfly sleeve oven (Phoenix S&T, Philadelphia, USA). The samples were run with a pre-programmed proprietary Evosep gradient of 44 min (30 samples per day) using water and 0.1% formic acid and solvent B acetonitrile and 0.1% formic acid as solvents. The LC was coupled to an Orbitrap Exploris 480 (Thermo Fisher Scientific, Bremen, Germany) using PepSep Sprayers and a Proxeon nanospray source. The peptides were introduced into the mass spectrometer via a PepSep Emitter 360-µm outer diameter × 20-µm inner diameter, heated at 300°C, and a spray voltage of 2 kV was applied. The injection capillary temperature was set at 300°C. The radio frequency ion funnel was set to 30%. For DIA data acquisition with endurance column, full scan mass spectrometry (MS) spectra with a mass range of 350–1650 m/z were acquired in profile mode in the Orbitrap with a resolution of 120,000 FWHM. The default charge state was set to 2+, and the filling time was set at a maximum of 60 ms with a limitation of 3 × 106 ions. DIA scans were acquired with 40 mass window segments of differing widths across the MS1 mass range. Higher collisional dissociation fragmentation (normalized collision energy 29%) was applied, and MS/MS spectra were acquired with a resolution of 30,000 FWHM with a fixed first mass of 200 m/z after accumulation of 1 × 106 ions or after filling time of 45 ms (whichever occurred first). Data were acquired in profile mode. For DIA data acquisition for Performance column, full scan mass spectrometry (MS) spectra with a mass range of 350–1650 m/z were acquired in profile mode in the Orbitrap with a resolution of 120,000 FWHM. The default charge state was set to 2+, and the filling time was set at a maximum of 20 ms with a limitation of 3 × 106 ions. DIA scans were acquired with 45 mass window segments of differing widths across the MS1 mass

range. Higher collisional dissociation fragmentation (normalized collision energy 30%) was applied, and MS/MS spectra were acquired with a resolution of 30,000 FWHM with a fixed first mass of 200 m/z after accumulation of 1 × 106 ions or after filling time of 45 ms (whichever occurred first). For data acquisition and processing of the raw data, Xcalibur 4.5 (Thermo) and Tune version 4.0 were used.

Proteomic data processing

DIA raw data were analysed using the directDIA pipeline in Spectronaut (v.17 and v.18, Biognosysis, Switzerland). The data were searched against an in house species-specific database (*N.furzeri*, 59154 entries, Nfu_20150522, annotation nfurzeri_genebuild_v1.150922) with a list of common contaminants appended (247 entries). The data were searched with the following variable modifications: oxidation (M) and acetyl (protein N-term). A maximum of 2 missed cleavages for trypsin and 5 variable modifications were allowed. The identifications were filtered to satisfy an FDR of 1% at the peptide and protein levels. Relative quantification was performed in Spectronaut for each paired comparison using the replicate samples from each condition. Precursors were percentile filtered at 0.2%. The data (candidate table) and data reports (protein quantities) were then exported, and further data analyses and visualization were performed with R studio using in-house pipelines and scripts. Differentially abundant proteins were defined as having a q-value <0.

Active avoidance test

We assessed the decline in learning ability of treated fish using an active avoidance behavioral test which was developed based on a test previously employed in killifish[37,39]. The setup consisted of two circular compartments connected through a small opening. Fish were acclimatized for 15 minutes in water from their home tank before testing began. A red light served as the conditioned stimulus, followed by air bubbles as the negative stimulus. Fish learned to avoid the negative stimulus by crossing the small opening into the opposite compartment when the red light appeared. The red light was presented for 30 seconds, with bubbles introduced after 15 seconds if the fish had not moved. Trials were counted as

'success' if the fish crossed the hurdle within 15 seconds of the red-light onset (before the introduction of bubbles). The cycle of stimulus, bubbles, and rest repeated 40 times per fish. Each fish underwent the test individually and was sacrificed immediately afterward. The entire test lasted one hour per animal. The water temperature was kept stable between 26.5°C and 28.0°C using a standard aquarium heater, which was important as varying temperatures could impact the performance of the fish.

Hybridizing Chain Reaction

Probe pair pools targeting *fos* and *neun* transcripts were generated and validated as previously described[34,84]. The probe sequences can be found in **Table S5**. The selected probe pairs were ordered from Integrated DNA Technologies, Inc. (IDT). The HCR protocol (HCRv3.0) was followed as previously published[85] with adaptations for cryosections as described by Van Houcke et al. (2021)[24]. Cryosections of 10um thick were used. The amplification of the signal was done for *fos* transcripts with HCR Amplifier B1, Alexa Fluor 647 and *neun* transcripts with HCR Amplifier B2, Alexa Fluor 546. Imaging was done with the Zeiss Axio Scan.Z1 microscope with a Plan-Apochromat 20x/0.8 M27 objective, Axiocam 506m imaging device and 1x Camera Adapter.

Acknowledgements

The FLI is a member of the Leibniz Association and is financially supported by the Federal Government of Germany and the State of Thuringia. The authors gratefully acknowledge support from the following FLI Core Facilities; CF Proteomics Facility, CF Imaging, CF Histology & Electron Microscopy, CF Next Generation Sequencing. In addition, we would like the acknowledge the Animal fish Facility of the FLI, with a special mention of Johannes Wilfert, as well as the fish facility of MPI-AGE. We also acknowledge the invaluable support from the Balance of the Microverse cluster in Jena. In addition, we would like to thank the group of Lutgarde Arckens at K.U. Leuven (Belgium), and especially Caroline Zandecki, for the help with setting up the hybridizing chain reaction experiment. In addition, we would like to thank the group of Randal Halfmann (Stowers Institute) for the expert advice and help with the interpretation of the data, as well as Mario Baumgart for his help with importing the *appa* mutant line to the FLI. D.E.M. de Bakker was financed by a Rubicon scholarship (452021116) from the Dutch Research Council (NWO) as well as by a research grant from the "Balance of the Microverse" Excellence Cluster from the Friedrich Schiller University in Jena.

Data availability

The produced transcriptomic datasets will be made publicly available at the Gene Expression Omnibus from NCBI. Proteomics data will be made publicly available at MassIVE, which can be found following the links below. Proteomics data for Young (6 weeks) versus Old (6 months) *N. furzeri* brains:

http://massive.ucsd.edu/ProteoSAFe/status.jsp?task=650a5a2e981540359f34b145717d2f7b

Proteomics data for *N. furzeri appa* -/- versus *appa* +/+ brains:

http://massive.ucsd.edu/ProteoSAFe/status.jsp?task=e7c08aa99a7a427c8ec6eb2623a9e5ec

Declaration of interests

The authors declare no competing interests.

Author contributions

DdB: Conceptualization, Formal Analysis, Investigation, Writing – Original Draft, Writing – Review & Editing, Project Administration, Funding Acquisition. **MM**: Formal Analysis, Investigation, Review & Editing. **KG**: Formal Analysis, Investigation, Review & Editing. **YR**: Formal Analysis, Investigation. **FB**: Formal Analysis, Investigation, Review & Editing. **LA**: Investigation. **FSS**: Investigation. **OO**: Formal Analysis, Investigation, Review & Editing, Visualization. **MB**: Formal Analysis, Investigation. **EC**: Formal Analysis, Investigation. **AA**: Resources. **IM**: Resources. **AS**: Conceptualization. **BS**: Supervision, Writing – Review & Editing. **JK**: Supervision, Writing – Review & Editing. **DRV**: Conceptualization, Writing – Original Draft, Writing – Review & Editing, Supervision, Project Administration, Funding Acquisition.

Bibliography

1. Wyss-Coray, T. Ageing, neurodegeneration and brain rejuvenation. *Nature* vol. 539 Preprint at https://doi.org/10.1038/nature20411 (2016).
2. Pluvinage, J. V. & Wyss-Coray, T. Systemic factors as mediators of brain homeostasis, ageing and neurodegeneration. *Nat Rev Neurosci* **21**, 93–102 (2020).
3. de Bakker, D. E. M. & Valenzano, D. R. Turquoise killifish: A natural model of age-dependent brain degeneration. *Ageing Res Rev* **90**, (2023).
4. Murphy, M. P. & Levine, H. Alzheimer's Disease and the β-Amyloid Peptide. *J Alzheimers Dis* **19**, 311 (2010).
5. Sehar, U., Rawat, P., Reddy, A. P., Kopel, J. & Reddy, P. H. Amyloid Beta in Aging and Alzheimer's Disease. *Int J Mol Sci* **23**, (2022).
6. Alvarez, J., Alvarez-Illera, P., Santo-Domingo, J., Fonteriz, R. I. & Montero, M. Modeling Alzheimer's Disease in Caenorhabditis elegans. *Biomedicines* **10**, (2022).
7. Gallrein, C. *et al.* Novel amyloid-beta pathology C. elegans model reveals distinct neurons as seeds of pathogenicity. *Prog Neurobiol* **198**, (2021).
8. O'Keefe, L. & Denton, D. Using Drosophila Models of Amyloid Toxicity to Study Autophagy in the Pathogenesis of Alzheimer's Disease. *BioMed Research International* vol. 2018 Preprint at https://doi.org/10.1155/2018/5195416 (2018).
9. Iijima, K. *et al.* Dissecting the pathological effects of human Aβ40 and Aβ42 in Drosophila: A potential model for Alzheimer's disease. *Proc Natl Acad Sci U S A* **101**, 6623–6628 (2004).
10. Forner, S. *et al.* Systematic phenotyping and characterization of the 5xFAD mouse model of Alzheimer's disease. *Scientific Data 2021 8:1* **8**, 1–16 (2021).
11. Yokoyama, M., Kobayashi, H., Tatsumi, L. & Tomita, T. Mouse Models of Alzheimer's Disease. *Front Mol Neurosci* **15**, (2022).
12. Poon, C. H., Wang, Y., Fung, M. L., Zhang, C. & Lim, L. W. Rodent Models of Amyloid-Beta Feature of Alzheimer's Disease: Development and Potential Treatment Implications. *Aging Dis* **11**, 1235 (2020).
13. Zhang, Y., Chen, H., Li, R., Sterling, K. & Song, W. Amyloid β-based therapy for Alzheimer's disease: challenges, successes and future. *Signal Transduction and Targeted Therapy 2023 8:1* **8**, 1–26 (2023).
14. van Dyck, C. H. *et al.* Lecanemab in Early Alzheimer's Disease. *N Engl J Med* (2022) doi:10.1056/NEJMOA2212948/SUPPL_FILE/NEJMOA2212948_APPENDIX.PDF.
15. Cummings, J. Anti-Amyloid Monoclonal Antibodies are Transformative Treatments that Redefine Alzheimer's Disease Therapeutics. *Drugs* **83**, 569–576 (2023).
16. Budd Haeberlein, S. *et al.* Two Randomized Phase 3 Studies of Aducanumab in Early Alzheimer's Disease. *Journal of Prevention of Alzheimer's Disease* **9**, 197–210 (2022).
17. Swanson, C. J. *et al.* A randomized, double-blind, phase 2b proof-of-concept clinical trial in early Alzheimer's disease with lecanemab, an anti-Aβ protofibril antibody. *Alzheimers Res Ther* **13**, (2021).
18. Sevigny, J. *et al.* The antibody aducanumab reduces Aβ plaques in Alzheimer's disease. *Nature 2016 537:7618* **537**, 50–56 (2016).
19. Ruparelia, A. A. *et al.* The African killifish: A short-lived vertebrate model to study the biology of sarcopenia and longevity. *Aging Cell* **23**, e13862 (2024).

20. Di Cicco, E., Tozzini, E. T., Rossi, G. & Cellerino, A. The short-lived annual fish Nothobranchius furzeri shows a typical teleost aging process reinforced by high incidence of age-dependent neoplasias. *Exp Gerontol* **46**, 249–256 (2011).
21. Reichard, M. *et al.* Lifespan and telomere length variation across populations of wild-derived African killifish. *Mol Ecol* **31**, 5979–5992 (2022).
22. Hartmann, N. *et al.* Telomeres shorten while Tert expression increases during ageing of the short-lived fish Nothobranchius furzeri. *Mech Ageing Dev* **130**, 290–296 (2009).
23. Wendler, S., Hartmann, N., Hoppe, B. & Englert, C. Age-dependent decline in fin regenerative capacity in the short-lived fish Nothobranchius furzeri. *Aging Cell* **14**, (2015).
24. Van houcke, J. *et al.* Aging impairs the essential contributions of non-glial progenitors to neurorepair in the dorsal telencephalon of the Killifish Nothobranchius furzeri. *Aging Cell* **20**, (2021).
25. Morabito, G., Ryabova, A. & Valenzano, D. R. Immune aging in annual killifish. *Immun Ageing* **21**, 18 (2024).
26. Bradshaw, W. J., Poeschla, M., Placzek, A., Kean, S. & Valenzano, D. R. Extensive age-dependent loss of antibody diversity in naturally short-lived turquoise killifish. *Elife* **11**, (2022).
27. Morabito, G. *et al.* Spontaneous onset of cellular markers of inflammation and genome instability during aging in the immune niche of the naturally short-lived turquoise killifish (Nothobranchius furzeri). *bioRxiv* 2023.02.06.527346 (2023) doi:10.1101/2023.02.06.527346.
28. Kelmer Sacramento, E. *et al.* Reduced proteasome activity in the aging brain results in ribosome stoichiometry loss and aggregation. *Mol Syst Biol* (2020) doi:10.15252/msb.20209596.
29. Matsui, H., Kenmochi, N. & Namikawa, K. Age- and α-Synuclein-Dependent Degeneration of Dopamine and Noradrenaline Neurons in the Annual Killifish Nothobranchius furzeri. *Cell Rep* **26**, 1727-1733.e6 (2019).
30. Louka, A. *et al.* New lessons on TDP-43 from old N. furzeri killifish. *Aging Cell* **21**, (2022).
31. Chen, Y. R. *et al.* Tissue-specific landscape of protein aggregation and quality control in an aging vertebrate. *Dev Cell* **0**, (2024).
32. Harel, I. *et al.* Identification of protein aggregates in the aging vertebrate brain with prion-like and phase-separation properties. *Cell Rep* **43**, (2024).
33. Tozzini, E. T., Baumgart, M., Battistoni, G. & Cellerino, A. Adult neurogenesis in the short-lived teleost Nothobranchius furzeri: Localization of neurogenic niches, molecular characterization and effects of aging. *Aging Cell* **11**, 241–251 (2012).
34. Vanhunsel, S. *et al.* The killifish visual system as an in vivo model to study brain aging and rejuvenation. *NPJ Aging Mech Dis* **7**, (2021).
35. Bagnoli, S., Fronte, B., Bibbiani, C., Terzibasi Tozzini, E. & Cellerino, A. Quantification of noradrenergic-, dopaminergic-, and tectal-neurons during aging in the short-lived killifish Nothobranchius furzeri. *Aging Cell* **21**, (2022).
36. Terzibasi, E. *et al.* Large differences in aging phenotype between strains of the short-lived annual fish Nothobranchius furzeri. *PLoS One* **3**, (2008).
37. Valenzano, D. R. *et al.* Resveratrol prolongs lifespan and retards the onset of age-related markers in a short-lived vertebrate. *Current Biology* **16**, 296–300 (2006).

38. McKay, A. *et al.* An automated feeding system for the African killifish reveals effects of dietary restriction on lifespan and allows scalable assessment of associative learning. *Elife* **11**, (2022).
39. Valenzano, D. R., Terzibasi, E., Cattaneo, A., Domenici, L. & Cellerino, A. Temperature affects longevity and age-related locomotor and cognitive decay in the short-lived fish: Nothobranchius furzeri. *Aging Cell* **5**, 275–278 (2006).
40. Bergmans, S., Raes, L., Moons, L. & De Groef, L. A review on neurodegeneration in the fast-ageing killifish, the first animal model to study the natural occurrence of neuronal cell loss. *Ageing Res Rev* **91**, (2023).
41. Scheidt, H. A. *et al.* Pyroglutamate-Modified Amyloid β (11- 40) Fibrils Are More Toxic than Wildtype Fibrils but Structurally Very Similar. *Chemistry - A European Journal* **23**, 15834–15838 (2017).
42. Bayer, T. A. Pyroglutamate Aβ cascade as drug target in Alzheimer's disease. *Molecular Psychiatry 2021 27:4* **27**, 1880–1885 (2021).
43. D'Angelo, L. Brain atlas of an emerging teleostean model: Nothobranchius furzeri. *Anatomical Record* **296**, 681–691 (2013).
44. Jucker, M. *et al.* Age-related deposition of glia-associated fibrillar material in brains of C57BL/6 mice. *Neuroscience* **60**, 875–889 (1994).
45. Jucker, M. *et al.* Age-associated inclusions in normal and transgenic mouse brain. *Science* **255**, 1443–1445 (1992).
46. Crowhurst, M. O., Layton, J. & Lieschke, G. Developmental biology of zebrafish myeloid cells. *International Journal of Developmental Biology* (2002) doi:10.1387/IJDB.12141435.
47. LaFerla, F. M., Green, K. N. & Oddo, S. Intracellular amyloid-β in Alzheimer's disease. *Nature Reviews Neuroscience 2007 8:7* **8**, 499–509 (2007).
48. Wegiel, J. *et al.* Intraneuronal Abeta immunoreactivity is not a predictor of brain amyloidosis-beta or neurofibrillary degeneration. *Acta Neuropathol* **113**, 389–402 (2007).
49. Oddo, S., Caccamo, A., Smith, I. F., Green, K. N. & LaFerla, F. M. A Dynamic Relationship between Intracellular and Extracellular Pools of Aβ. *Am J Pathol* **168**, 184 (2006).
50. Mori, C. *et al.* Intraneuronal Aβ42 accumulation in Down syndrome brain. *Amyloid* **9**, 88–102 (2002).
51. Gyure, K. A., Durham, R., Stewart, W. F., Smialek, J. E. & Troncoso, J. C. Intraneuronal abeta-amyloid precedes development of amyloid plaques in Down syndrome. *Arch Pathol Lab Med* **125**, 489–492 (2001).
52. Lee, J. H. *et al.* Faulty autolysosome acidification in Alzheimer's disease mouse models induces autophagic build-up of Aβ in neurons, yielding senile plaques. *Nature Neuroscience 2022 25:6* **25**, 688–701 (2022).
53. He, W. & Barrow, C. J. The A beta 3-pyroglutamyl and 11-pyroglutamyl peptides found in senile plaque have greater beta-sheet forming and aggregation propensities in vitro than full-length A beta. *Biochemistry* **38**, 10871–10877 (1999).
54. Cynis, H., Scheel, E., Saido, T. C., Schilling, S. & Demuth, H. U. Amyloidogenic processing of amyloid precursor protein: Evidence of a pivotal role of glutaminyl cyclase in generation of pyroglutamate-modified amyloid-β. *Biochemistry* **47**, 7405–7413 (2008).

55. Kalimo, H. *et al.* The Arctic AβPP mutation leads to Alzheimer's disease pathology with highly variable topographic deposition of differentially truncated Aβ. *Acta Neuropathol Commun* **2**, 1–19 (2014).
56. Hartlage-Rübsamen, M. *et al.* Glutaminyl cyclase contributes to the formation of focal and diffuse pyroglutamate (pGlu)-Aβ deposits in hippocampus via distinct cellular mechanisms. *Acta Neuropathol* **121**, 705–719 (2011).
57. Kirby, M., Yu, D. M. T., O'Connor, S. P. & Gorrell, M. D. Inhibitor selectivity in the clinical application of dipeptidyl peptidase-4 inhibition. *Clin Sci (Lond)* **118**, 31–41 (2009).
58. Xue, C., Lin, T. Y., Chang, D. & Guo, Z. Thioflavin T as an amyloid dye: fibril quantification, optimal concentration and effect on aggregation. *R Soc Open Sci* **4**, (2016).
59. Scior, A. *et al.* Complete suppression of Htt fibrilization and disaggregation of Htt fibrils by a trimeric chaperone complex. *EMBO J* **37**, 282–299 (2018).
60. Banote, R. K. *et al.* Amyloid precursor protein-b facilitates cell adhesion during early development in zebrafish. *Sci Rep* **10**, (2020).
61. Samali, A., Cai, J., Zhivotovsky, B., Jones, D. P. & Orrenius, S. *Presence of a Pre-Apoptotic Complex of pro-Caspase-3, Hsp60 and Hsp10 in the Mitochondrial Fraction of Jurkat Cells*. *The EMBO Journal* vol. 18 (1999).
62. Piront, M. L. & Schmidt, R. Inhibition of long-term memory formation by anti-ependymin antisera after active shock-avoidance learning in goldfish. *Brain Res* **442**, 53–62 (1988).
63. Inhibition of memory consolidation by antibodies against cell adhesion molecules after active avoidance conditioning in zebrafish - PubMed. https://pubmed.ncbi.nlm.nih.gov/10235674/.
64. Lin, X. *et al.* c-Fos mapping of brain regions activated by multi-modal and electric foot shock stress. *Neurobiol Stress* **8**, 92–102 (2018).
65. Lara Aparicio, S. Y. *et al.* Current Opinion on the Use of c-Fos in Neuroscience. *NeuroSci* **3**, 687–702 (2022).
66. Calvo, R., Hofmann, M. H. & Schluessel, V. Brain areas activated during visual learning in the cichlid fish Pseudotropheus zebra. *Brain Struct Funct* **228**, 859–873 (2023).
67. Maloney, J. A. *et al.* Molecular Mechanisms of Alzheimer Disease Protection by the A673T Allele of Amyloid Precursor Protein. *J Biol Chem* **289**, 30990 (2014).
68. Jonsson, T. *et al.* A mutation in APP protects against Alzheimer's disease and age-related cognitive decline. *Nature 2012 488:7409* **488**, 96–99 (2012).
69. Cui, R. *et al.* Relaxed Selection Limits Lifespan by Increasing Mutation Load. *Cell* **178**, 385-399.e20 (2019).
70. Wittnam, J. L. *et al.* Pyroglutamate Amyloid β (Aβ) Aggravates Behavioral Deficits in Transgenic Amyloid Mouse Model for Alzheimer Disease. *J Biol Chem* **287**, 8154 (2012).
71. Luheshi, L. M. *et al.* Sequestration of the Aβ peptide prevents toxicity and promotes degradation in vivo. *PLoS Biol* **8**, (2010).
72. Wang, S. *et al.* Amyloid β precursor protein regulates neuron survival and maturation in the adult mouse brain. *Molecular and Cellular Neuroscience* **77**, 21–33 (2016).
73. Zheng, H. *et al.* beta-Amyloid precursor protein-deficient mice show reactive gliosis and decreased locomotor activity. *Cell* **81**, 525–531 (1995).
74. Senechal, Y., Kelly, P. H. & Dev, K. K. Amyloid precursor protein knockout mice show age-dependent deficits in passive avoidance learning. *Behavioural Brain Research* **186**, 126–132 (2008).

75. Morley, J. E., Farr, S. A., Nguyen, A. D. & Xu, F. What is the Physiological Function of Amyloid-Beta Protein? *Journal of Nutrition, Health and Aging* **23**, 225–226 (2019).
76. Glasauer, S. M. K. & Neuhauss, S. C. F. Whole-genome duplication in teleost fishes and its evolutionary consequences. *Molecular Genetics and Genomics* **289**, 1045–1060 (2014).
77. Naumann, U., Brazzell, J. L., Crim, M. J. & Hoppe, B. Comprehensive Colony Health Management and Emerging Pathogens of the Annual Killifish Species Nothobranchius furzeri. *J Am Assoc Lab Anim Sci* **63**, 20–33 (2024).
78. Abramson, J. *et al.* Accurate structure prediction of biomolecular interactions with AlphaFold 3. *Nature 2024 630:8016* **630**, 493–500 (2024).
79. Pettersen, E. F. *et al.* UCSF ChimeraX: Structure visualization for researchers, educators, and developers. *Protein Sci* **30**, 70–82 (2021).
80. Bentley, D. R. *et al.* Accurate whole human genome sequencing using reversible terminator chemistry. *Nature* **456**, 53–59 (2008).
81. Willemsen, D., Cui, R., Reichard, M. & Valenzano, D. R. Intra-species differences in population size shape life history and genome evolution. *Elife* **9**, 1–26 (2020).
82. Robinson, M. D., McCarthy, D. J. & Smyth, G. K. edgeR: a Bioconductor package for differential expression analysis of digital gene expression data. *Bioinformatics* **26**, 139–140 (2010).
83. Huang, D. W., Sherman, B. T. & Lempicki, R. A. Systematic and integrative analysis of large gene lists using DAVID bioinformatics resources. *Nature Protocols 2009 4:1* **4**, 44–57 (2008).
84. Elagoz, A. M. *et al.* Optimization of Whole Mount RNA Multiplexed in situ Hybridization Chain Reaction With Immunohistochemistry, Clearing and Imaging to Visualize Octopus Embryonic Neurogenesis. *Front Physiol* **13**, 882413 (2022).
85. Choi, H. M. T. *et al.* Third-generation in situ hybridization chain reaction: multiplexed, quantitative, sensitive, versatile, robust. *Development* **145**, (2018).

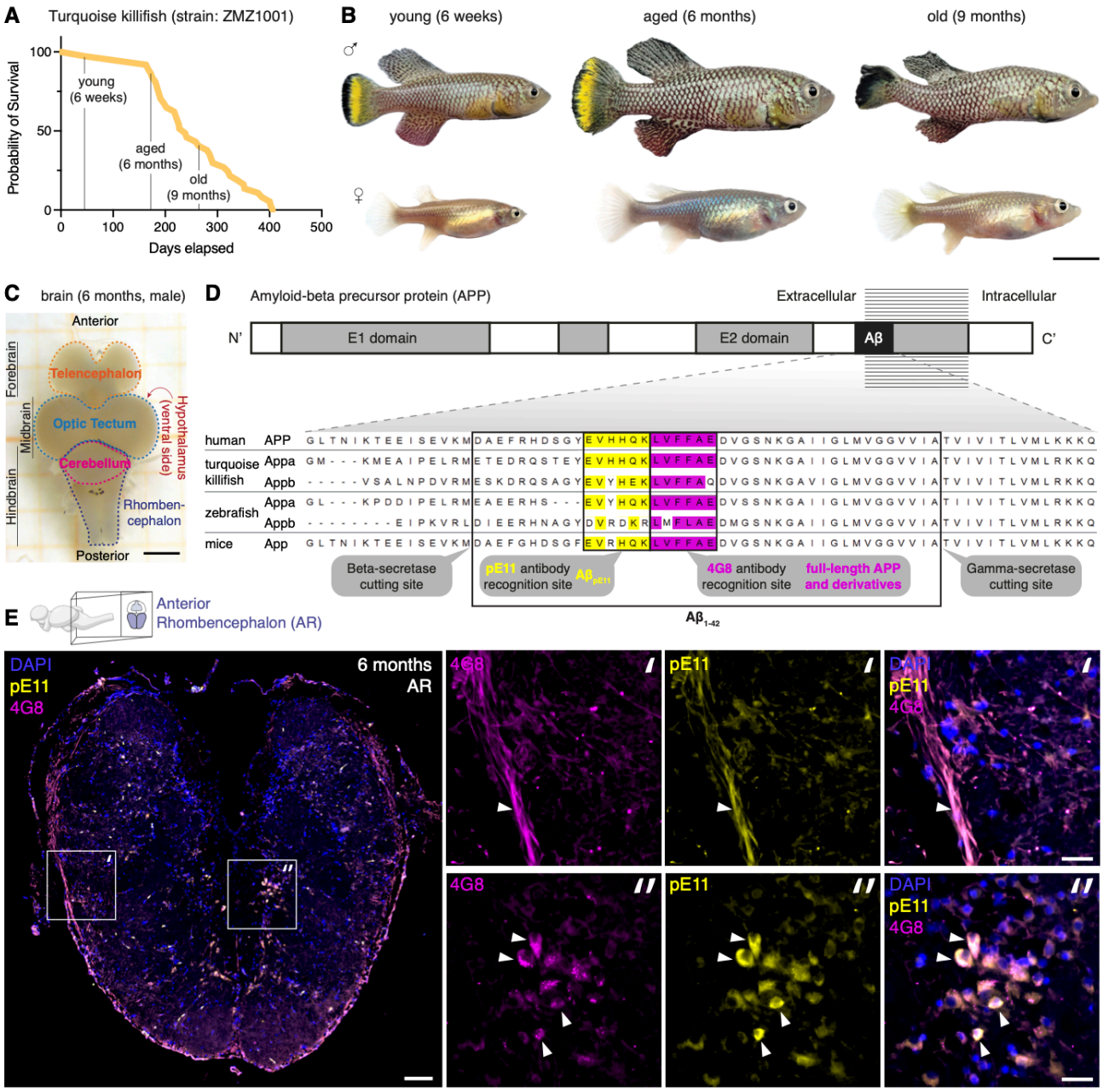

Figure 1. Amyloid beta is evolutionarily conserved between turquoise killifish and humans and is expressed in the turquoise killifish brain. (**A**) Survival curve for the turquoise killifish strain ZMZ1001. (**B**) Representative pictures of male and female fish at different ages. Scalebar represents 1 cm. (**C**) Representative brain (6-month-old male) with annotated brain regions. Scalebar represents 1 mm. (**D**) Graphical representation of the amyloid precursor protein (APP) and amino acid sequences of APP precursors across four species. Amino acid residues are colored according to their physicochemical properties (ZAPPO): aliphatic/hydrophobic (residues ILVAM) - rose, aromatic (FWY) - orange, positive (KRH) - dark blue, negative (DE) - red, hydrophilic (STNQ) - light green, conformationally special (PG) - magenta, cysteine (C) - yellow. (**E**) Immunohistochemistry staining in the 6-month-old anterior rhombencephalon (AR) using the pE11 and 4G8 antibodies, targeting $A\beta_{pE11\text{-}42}$ (yellow) and APP-derivatives (magenta), respectively. Arrowheads indicate pE11^{+}/4G8^{+} signal. Scalebars represent 100 μm in the overview and 25 μm in the zoom-ins.

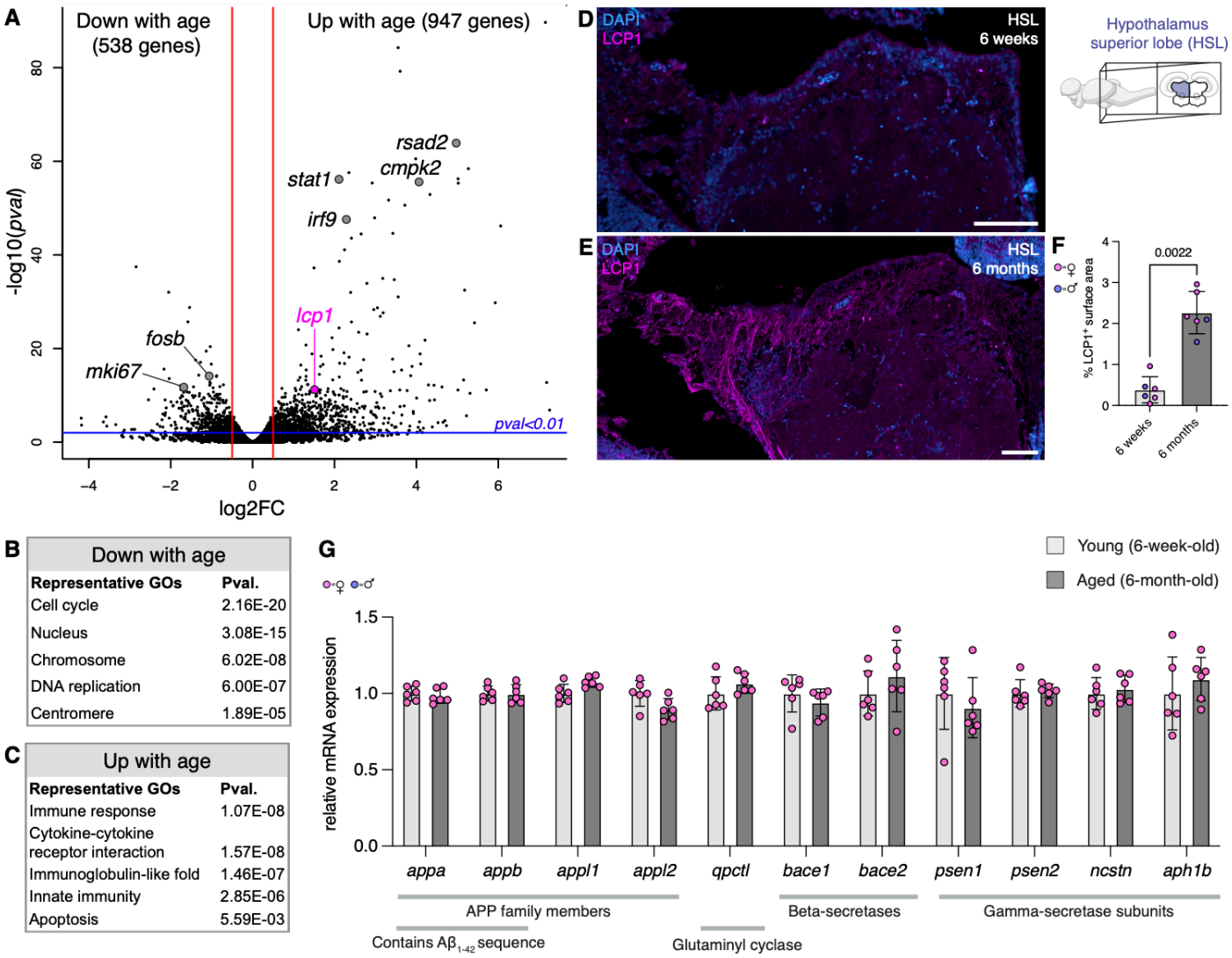

Figure 2. The turquoise killifish brain develops an age-related inflammatory state while expressing key players of Aβ biogenesis. (**A**) Volcano plot displaying differences in gene expression levels between young (6-week-old) and aged (6-month-old) female killifish brains. Differentially expressed genes are highlighted, representing relevant biological processes. Vertical red lines indicate (-)logFC of 0.5. (**B,C**) Representative gene ontologies produced from the differentially expressed genes between young and old brains (Log2FC > 0.5 / < -0.5 and pval < 0.01). (**D,E**) Immunohistochemistry staining targeting leukocyte marker Lymphocyte Cytosolic Protein 1 (LCP1) in sections of the hypothalamus superior lobe (HSL) from a young (D) and aged (E) individual. Scale bars represent 100 μm. (**F**) Quantification of the percentage of LCP1+ covered surface area in the hypothalamus of young and aged brains. Significance was calculated using a Mann-Whitney test. Error bars represent standard deviation. (**G**) Expression levels of key players in Aβ biogenesis normalized to total mRNA counts per brain, plotted as relative values to the mean value of young (6-week-old) individuals. APP = Amyloid beta Precursor Protein. Error bars represent standard deviation.

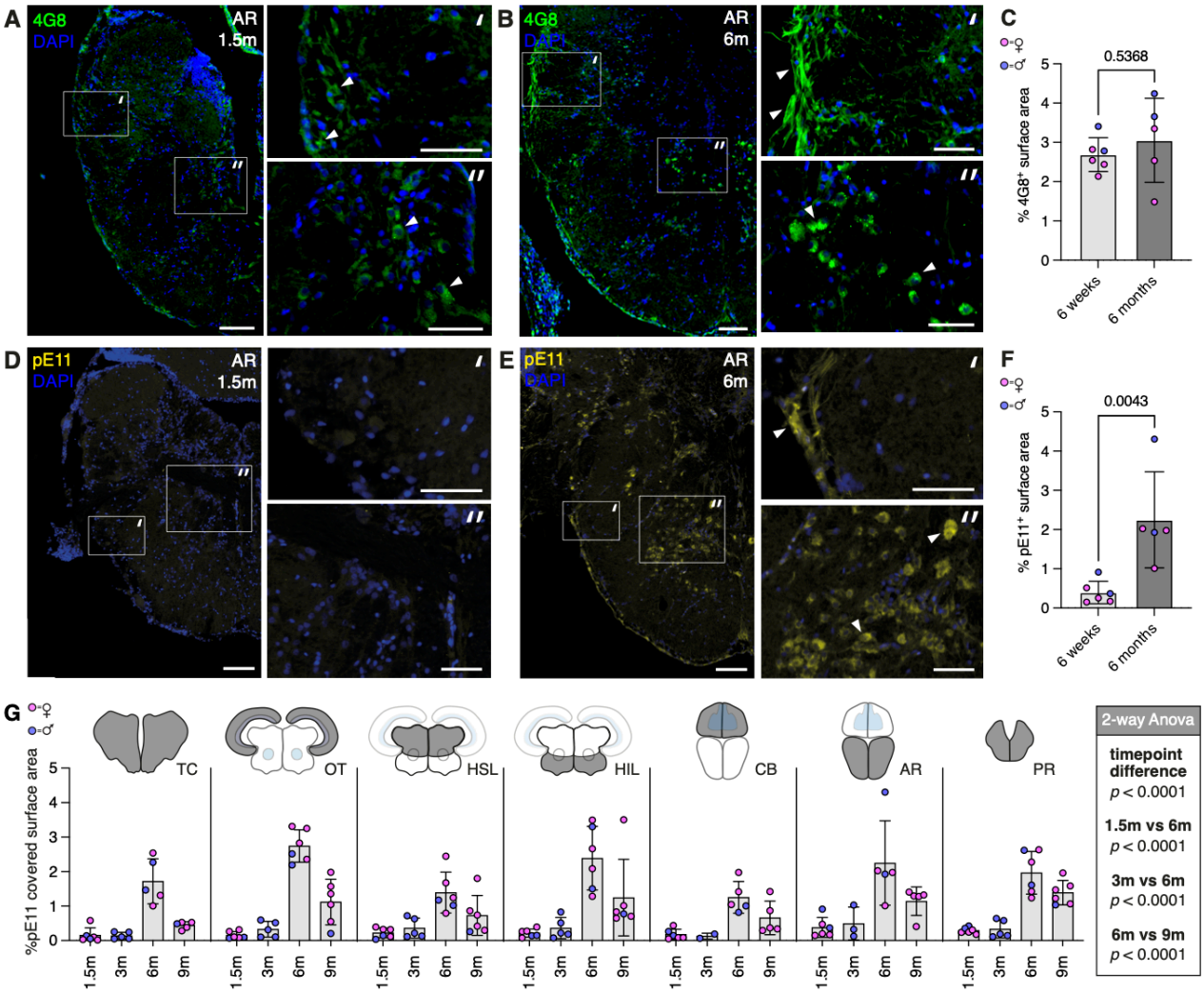

Figure 3. pE11 signal accumulates in an age-dependent manner across the rostrocaudal axis of the turquoise killifish brain. (**A,B**) Immunohistochemistry staining using the 4G8 antibody in the anterior rhombencephalon (AR) of young (6-week-old) and aged (6-month-old) killifish. (**C**) Quantification of the percentage of 4G8-covered surface area in 6-week-old and 6-month-old AR regions. Significance was calculated using a Mann-Whitney test. (**D,E**) Immunohistochemistry staining using the pE11 antibody in the anterior rhomboencephalon (AR) of young (6-week-old) and aged (6-month-old) killifish. (**F**) Quantification of the percentage of pE11-covered surface area in 6-week-old and 6-month-old AR regions. Significance was calculated using a Mann-Whitney test. (A, B, D, E) Scale bars represent 100 µm in the overview and 50 µm in the zoom-in. Arrowheads indicate positive signal. (C, F) Error bars represent standard deviation. (**G**) Quantification of the percentage of pE11-covered surface area across seven different brain regions at four different time points, including the telencephalon (TC), optic tectum (OT), hypothalamus superior lobe (HSL), hypothalamus inferior lobe (HIL), cerebellum (CB), anterior rhombencephalon (AR) and posterior rhombencephalon (PR). Error bars represent standard deviation. Significances were calculated using a 2-way Anova test, including a multiple comparison test to investigate the difference between 1.5-months and 6-months, 3-months and 6-months as well as 6-months and 9-months.

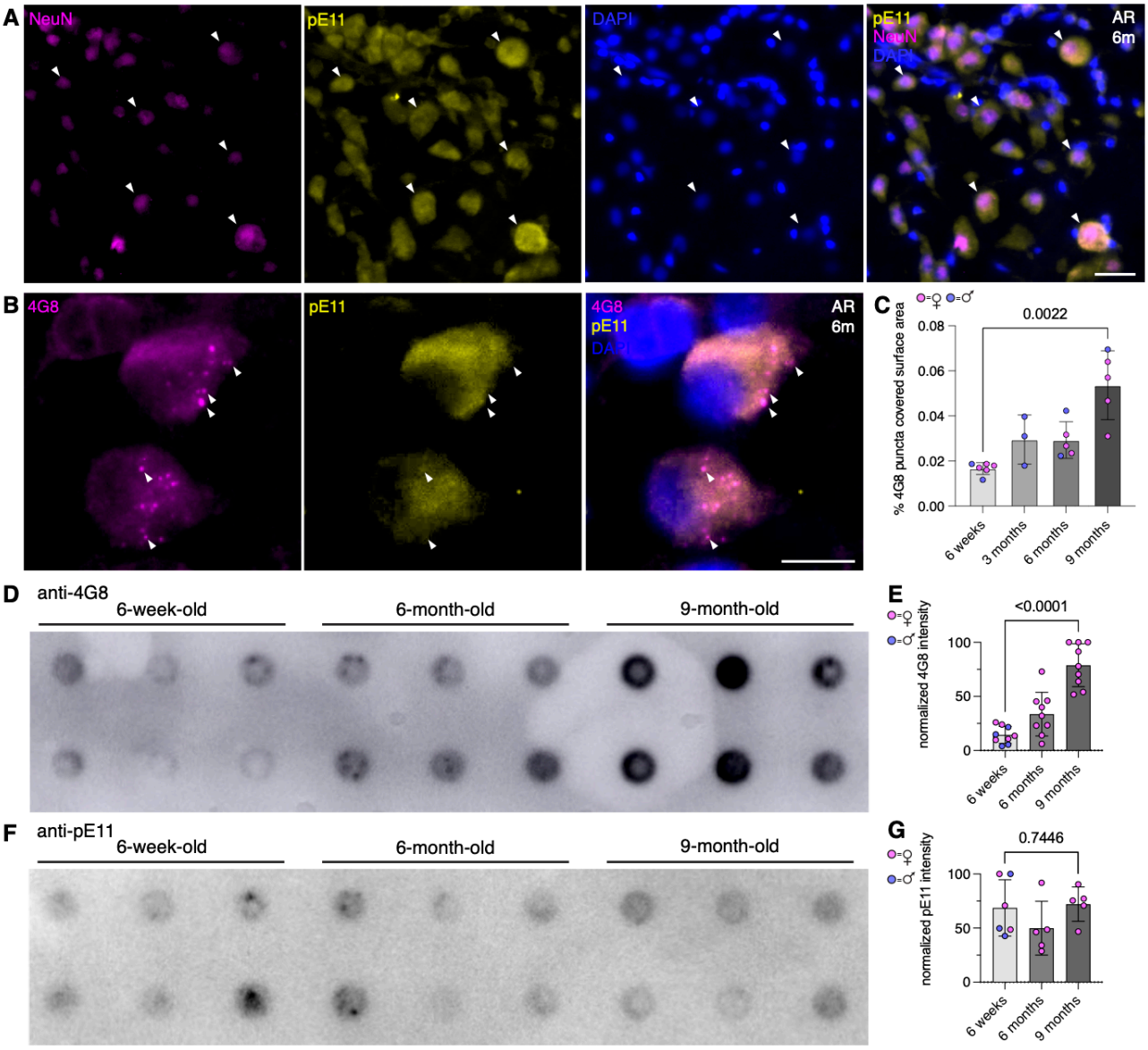

Figure 4. Intraneuronal 4G8⁺/pE11⁻ peptides show increased aggregation with age. (**A**) Immunohistochemistry staining in the 6-month-old anterior rhombencephalon (AR) using the pE11 antibody (yellow) and NeuN (Neuronal Nuclei) antibody. Arrowheads indicate colocalizing NeuN and pE11 signals. Scale bar represents 20 μm. (**B**) Immunohistochemistry staining in the 6-month-old AR using the pE11 antibody (yellow) and 4G8 antibody (magenta). Arrowheads indicate 4G8⁺/pE11⁻ puncta. Scale bar represents 10 μm. (**C**) Quantification of the percentage of 4G8⁺-puncta-covered surface area in AR regions at four different ages. Significance was calculated using a Mann-Whitney test. Error bars represent standard deviation. (**D**) Filter retardation analysis of 4G8⁺ aggregates. 100 μg of protein from brain lysates from three individual killifish of each age group was spotted on the filter in duplicates (top/bottom) and probed with an anti-4G8 antibody. (**E**) Quantification of 4G8⁺ signal normalized against the maximum value measured per experiment. Each dot represents the averaged value of three technical replicates per brain. Error bars represent standard deviation. Significance was calculated using a Mann-Whitney test. (**F**) Filter retardation analysis of pE11⁺ aggregates. 100 μg of protein from brain lysates from three individual killifish of each age group was spotted on the filter in duplicates (top/bottom) and probed with an anti-pE11 antibody. (**G**) Quantification of pE11⁺ signal normalized against the maximum value measured per experiment. Each dot represents the averaged value of three technical replicates per brain. Error bars represent standard deviation. Significance was calculated using a Mann-Whitney test.

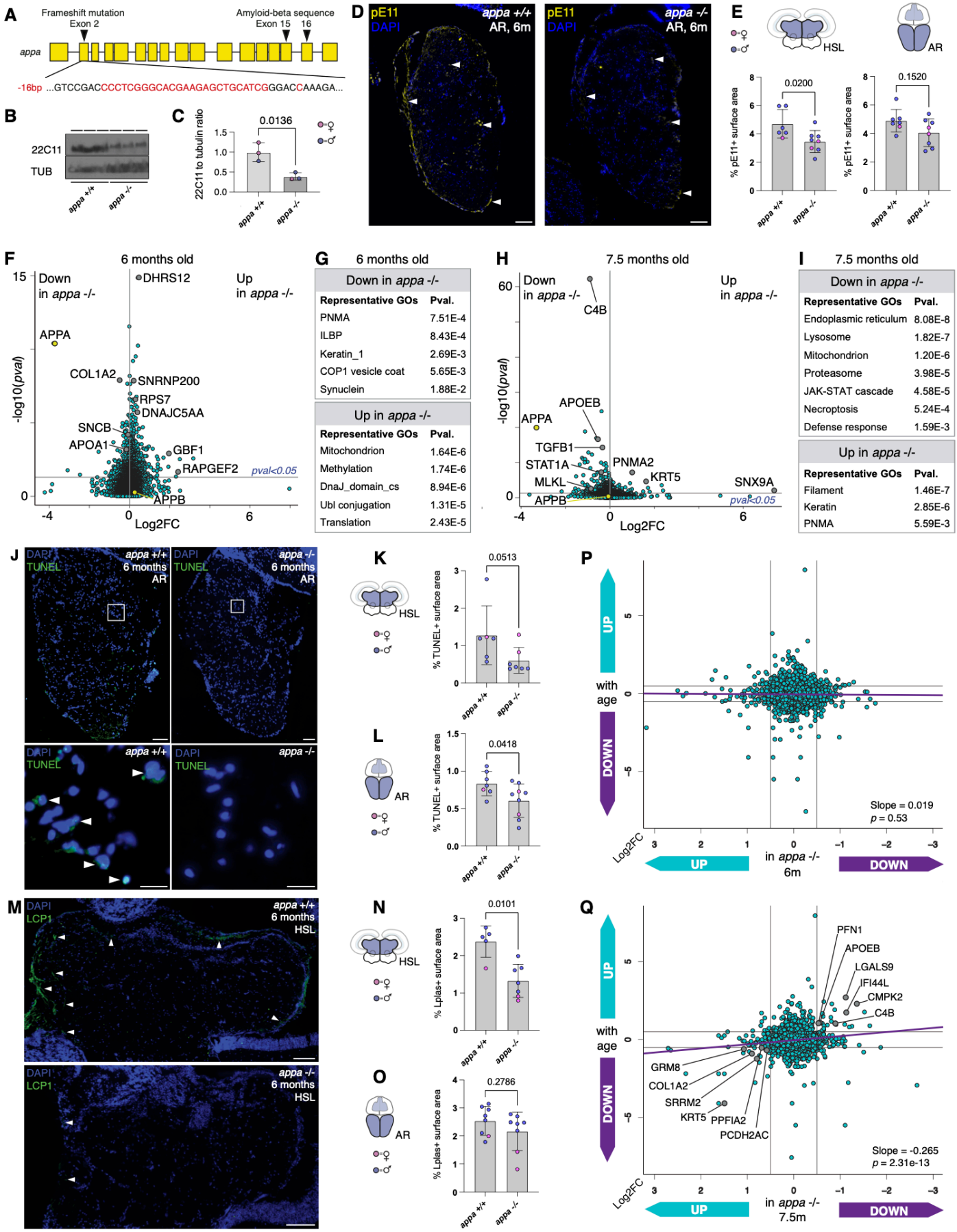

Figure 5. *appa* knock-out mitigates killifish brain aging including cell death and inflammation. (**A**) Schematic representation of the killifish *appa* gene, indicating the mutation site on exon 2, as well as highlighting the location of the amyloid beta coding region in exons 15 and 16.

(**B**) Western blot on turquoise killifish lysates from 6-month-old killifish using 22C11 and tubulin targeting antibodies. (**C**) Quantification of western blot results, depicting the 22C11 to tubulin ratio. Significance was calculated using a Mann-Whitney test. (**D**) Representative immunohistochemistry staining results using the pE11 antibody (yellow) in the anterior rhombencephalon (AR) of wild-type and *appa* -/- brains. Arrowheads indicate pE11$^+$ signal. Scale bar represents 100 μm. (**E**) Quantification of the percentage of pE11$^+$-puncta-covered surface area in hypothalamus superior lobe (HSL) and anterior rhomboencephalon (AR) regions of 6-month-old individuals. Significance was calculated using a Mann-Whitney test. Error bars represent standard deviation. (**F**) Volcano plot displaying differences in brain protein abundance between *appa* -/- and their wild-type siblings (6-month-old, 3 males and 3 females per genotype). Differentially abundant proteins are highlighted, representing relevant biological processes. Vertical red line indicates logFC of 0. (**G**) Representative gene ontologies produced from the differentially abundant proteins between 6-month-old *appa* -/- mutants and their wild-type siblings (pval < 0.05). (**H**) Volcano plot displaying differences in brain protein abundance between *appa* -/- mutants and their wild-type siblings (7.5-month-old, 3 males and 3 females per genotype). Differentially abundant proteins are highlighted, representing relevant biological processes. Vertical red line indicates logFC of 0. (**I**) Representative gene ontologies produced from the differentially abundant proteins between 7.5-month-old *appa* -/- mutants and their wild-type siblings (pval < 0.05). (**J**) Representative TUNEL (green) staining results in the anterior rhombencephalon (AR) of wild-type and *appa* -/- mutant brains. Arrowheads indicate TUNEL$^+$ signal. Scale bar represents 100 μm in the overview and 20 μm in the zoom-ins. (**K, L**) Quantification of the percentage of TUNEL$^+$-covered surface area in hypothalamus superior lobe (K) and anterior rhomboencephalon (L) regions of 6-month-old individuals. Significance was calculated using a Mann-Whitney test. Error bars represent standard deviation. (**M**) Representative immunohistochemistry staining results using the LCP1 antibody (green) in the hypothalamus superior lobe (HSL) of wild-type and *appa* -/- brains. Arrowheads indicate LCP1$^+$ signal. Scale bar represents 100 μm. (**N, O**) Quantification of the percentage of LCP1$^+$-covered surface area in hypothalamus superior lobe (N) and anterior rhombencephalon (O) regions of 6-month-old individuals (3 male, 3 female). Significance was calculated using a Mann-Whitney test. Error bars represent standard deviation. (**P, Q**) Proteome-wide comparison between the log2FC of proteins up or downregulated in 6-months-old brains compared to 6-weeks-old brains (y-axis), plotted against the log2FC describing the up and downregulation of proteins in the appa mutant compared to the same aged wild-type siblings at 6-months (P) and 7.5 months (Q).

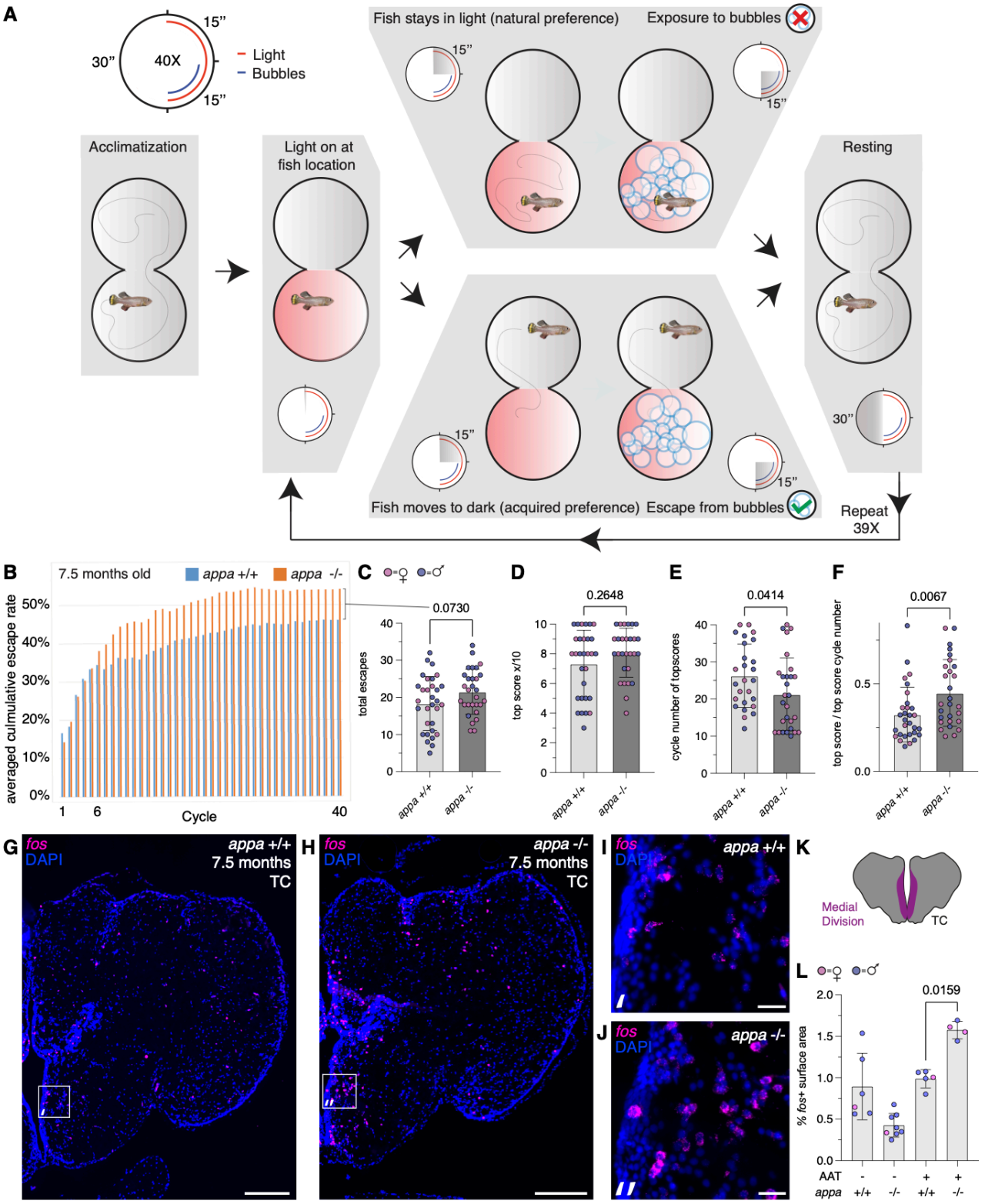

Figure 6. *appa* knock-out mitigates age-related learning deficiency in turquoise killifish. (**A**) Experimental set-up of the performed active avoidance test (AAT). (**B**) Plot describing the averaged cumulative escape rate of 7.5-month-old *appa* -/- mutants (orange, n = 28 fish) and their wild-type siblings (blue, n = 30 fish) across 40 cycles. (**C-F**) Quantification of four behavioral traits, compared between 7.5-month-old *appa* -/- mutants and their wild-type siblings. These traits include (**C**) the total escape rate (n/40 cycles), (**D**) the top score of the fish within a window of ten consecutive cycles representing the extent of learning, (**E**) the cycle number at which top scores were reached (excluding non-learners (n=4) defined by total escapes < 10) representing the speed of learning, and (**F**) a combined value in which both the extent and speed of learning were considered (top scores / cycle number at which top scores were reached). Significance values were calculated through Mann-Whitney testing. (**G-J**) Hybridizing Chain Reaction (HCR) staining against *fos* transcripts (magenta), marking neurons involved in active learning within the telencephalon (TC) of *appa* mutants (**H,J**) and their wild-type siblings (**G,I**). Scale bars represent 200 μm in the overview and 20 μm in the zoom-ins. (**K**) Schematic representation of the medial division (magenta) within the telencephalon (TC). (**L**) Quantification of the percentage of *fos*+ surface area in the medial division of the telencephalon of 6-month-old *appa* -/- mutant fish and their wild-type siblings that have not been subjected to an active avoidance test (AAT -), as well as as 7.5-month-old *appa* -/- mutant fish and their wild-type siblings which were subjected to an active avoidance test (AAT +). Significance value was calculated through a Mann-Whitney test.

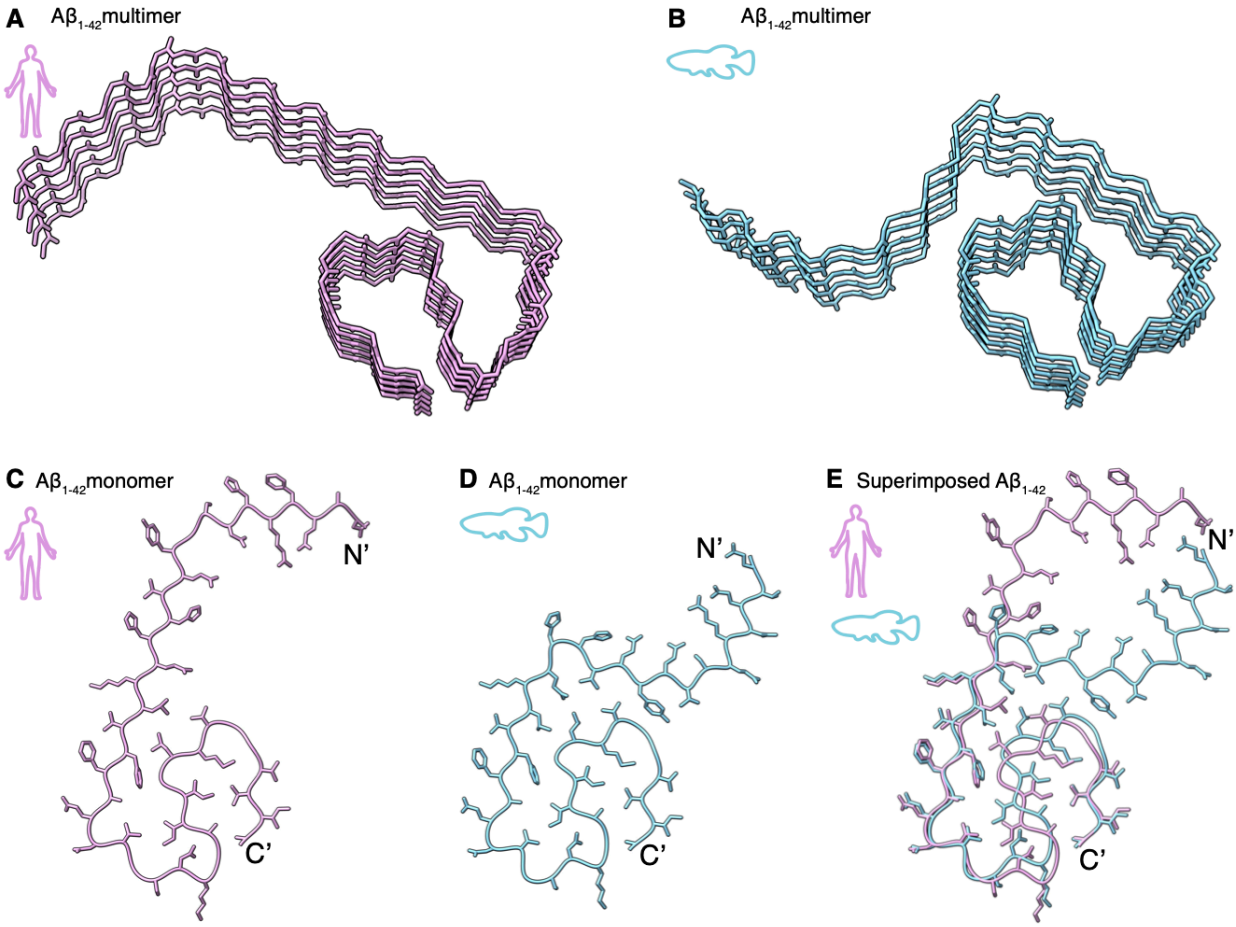

Figure S1. 3D protein structure of amyloid beta (1-42) is conserved between turquoise killifish and humans. (**A**) Alphafold (V3) predicted stucture of human amyloid beta (1-42) in an aggregated state. (**B**) Alphafold-predicted stucture of killifish amyloid beta (1-42) derived from *appa* in an aggregated state. (**C**) Alphafold prediction of human amyloid beta monomer 1-42), as part of the multimer shown in (A). (**D**) Alphafold prediction of turquoise killifish amyloid beta monomer (1-42) derived from *appa*, as part of the multimer shown in (B). (**E**) Superimposed of the Alphafold-predicted multimer structures (only one monomer displayed) of human (pink) and killifish (blue) amyloid beta (1-42) (backbone r.m.s.d. for residues Q15-A42: 0.859 Angstrom).

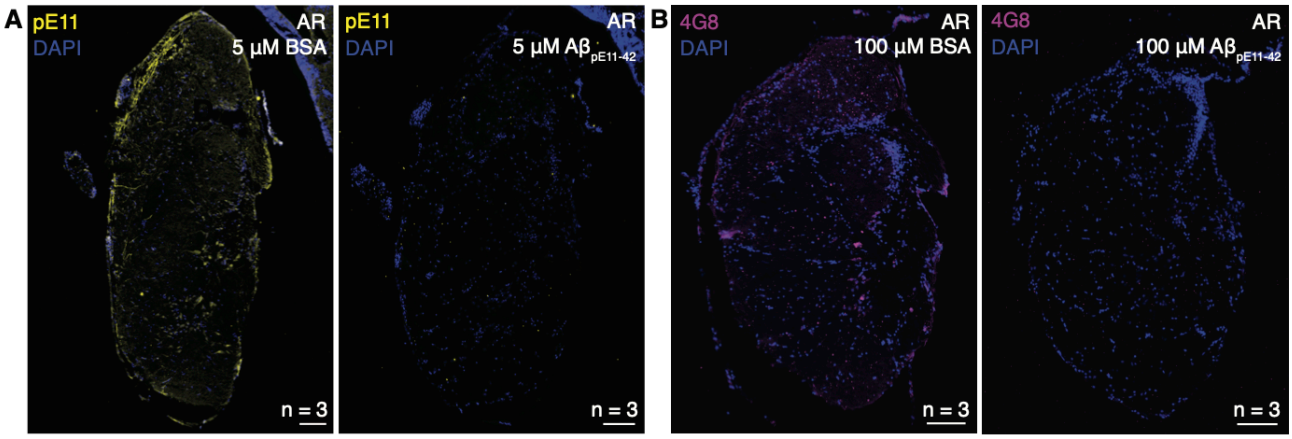

Figure S2. pE11 and 4G8 antibodies bind their targets in an epitope dependent manner. (A-B) Immunohistochemistry staining using the pE11 (A) or 4G8 (B) antibody, after a 30 minute incubation step of the primary antibody together with either BSA (left) or $A\beta_{pE11-42}$ peptide (right). The anterior rhombencephalon (AR) was stained from three 6-month-old turquoise killifish per condition. Scalebars represent 100 μm.

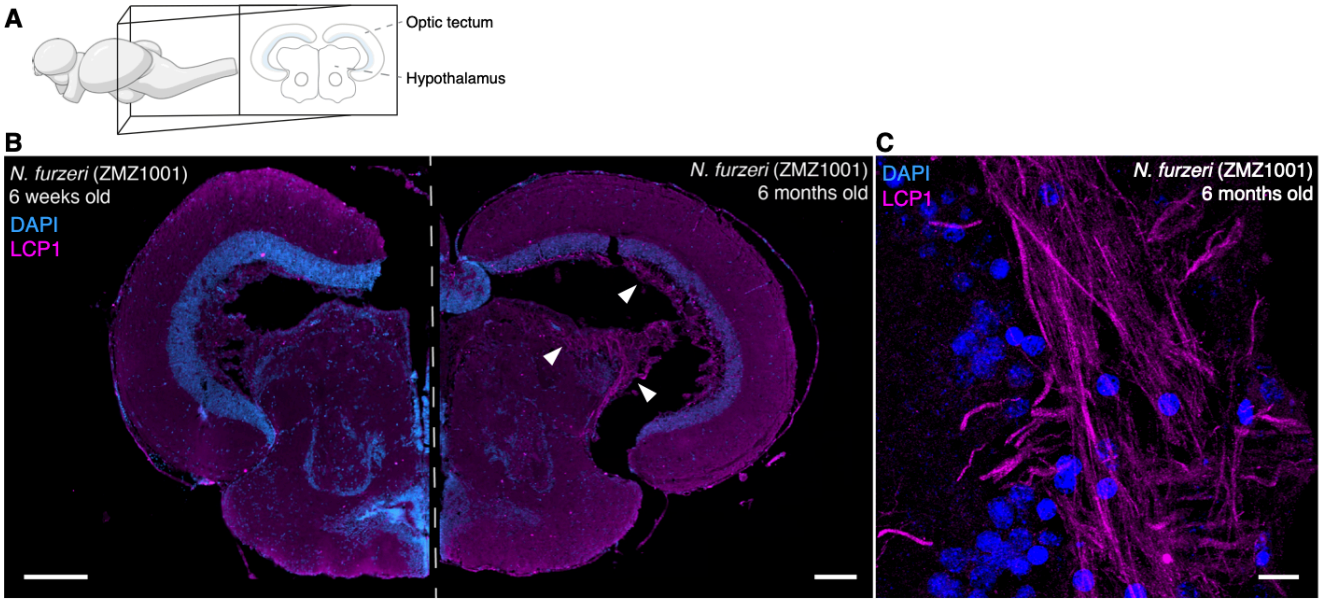

Figure S3. LCP1 antibody binds the actin cytoskeleton of leukocytes in the killifish brain. (**A**) Schematic representation of the brain region shown in B and C. (**B**) Immunohistochemistry staining targeting leukocyte marker Lymphocyte Cytosolic Protein 1 (LCP1, magenta) in sections of the optic tectum (OT) and hypothalamus superior lobe (HSL) from a young (left) and aged (right) individual. Scale bars represent 100 μm. Arrowheads indicate regions of high immunoreactivity. (**C**) High-resolution image of the HSL of a 6-month-old killifish brain, showing the striated pattern of the LCP1 staining, which reflects binding to the actin cytoskeleton. Scale bar represents 100 μm.

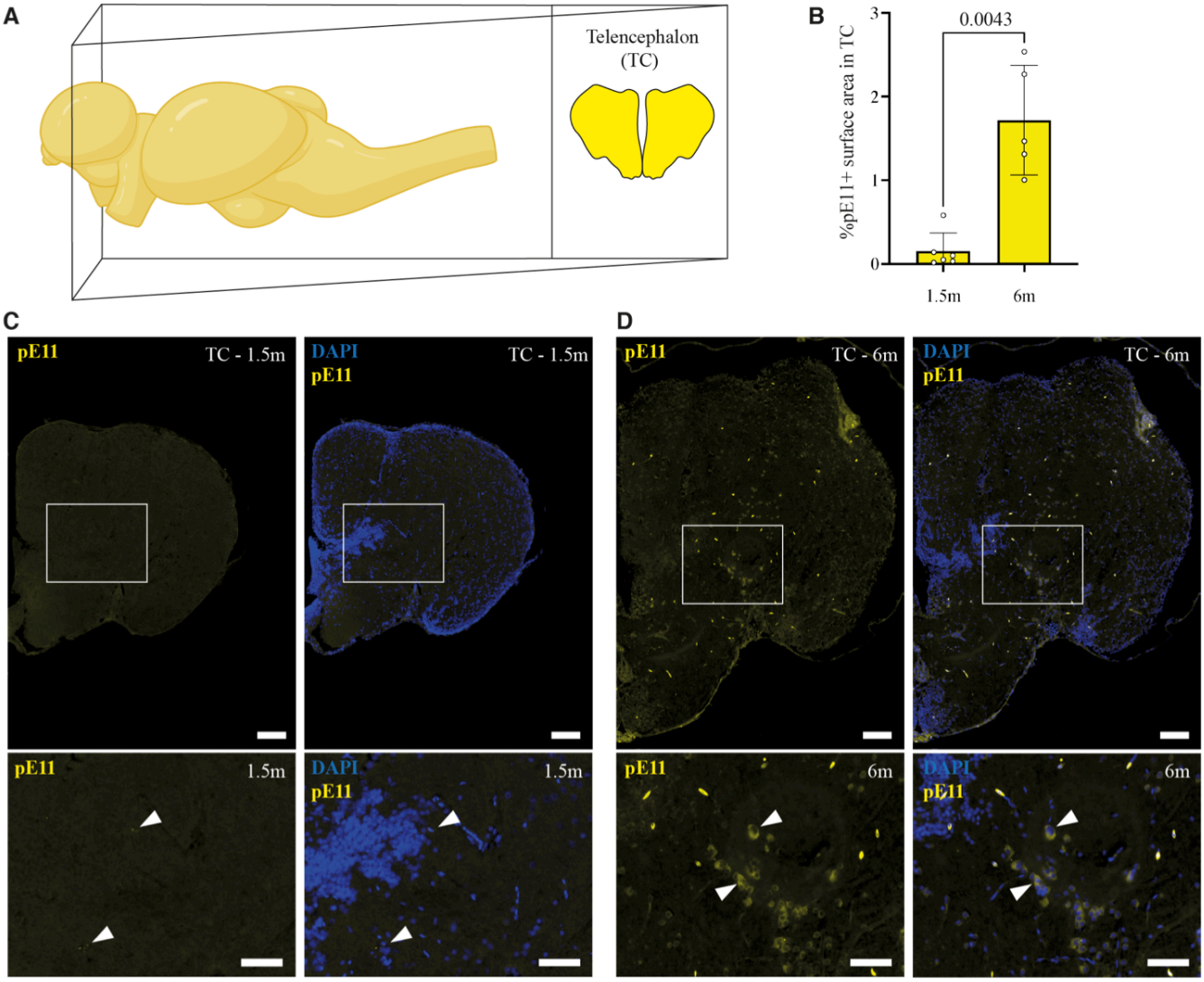

Figure S4. pE11 signal accumulates in the telencephalon in an age-dependent manner. (**A**) Schematic representation of the brain region quantified and shown in B-D. (**B**) Quantification of immunohistochemistry staining using the pE11 antibody on the telencephalon (TC) of young (6-week-old) and aged (6-month-old) killifish. Significance was calculated using a Mann-Whitney test. (**C, D**) Immunohistochemistry staining with the pE11 antibody (yellow) and DAPI (blue) in a 6-week-old (C) and 6-month-old (D) telencephalon. Arrowheads indicate examples of regions with perinuclear immunoreactivity. Scale bar represents 100 μm in the overview and 50 μm in the zoom-in.

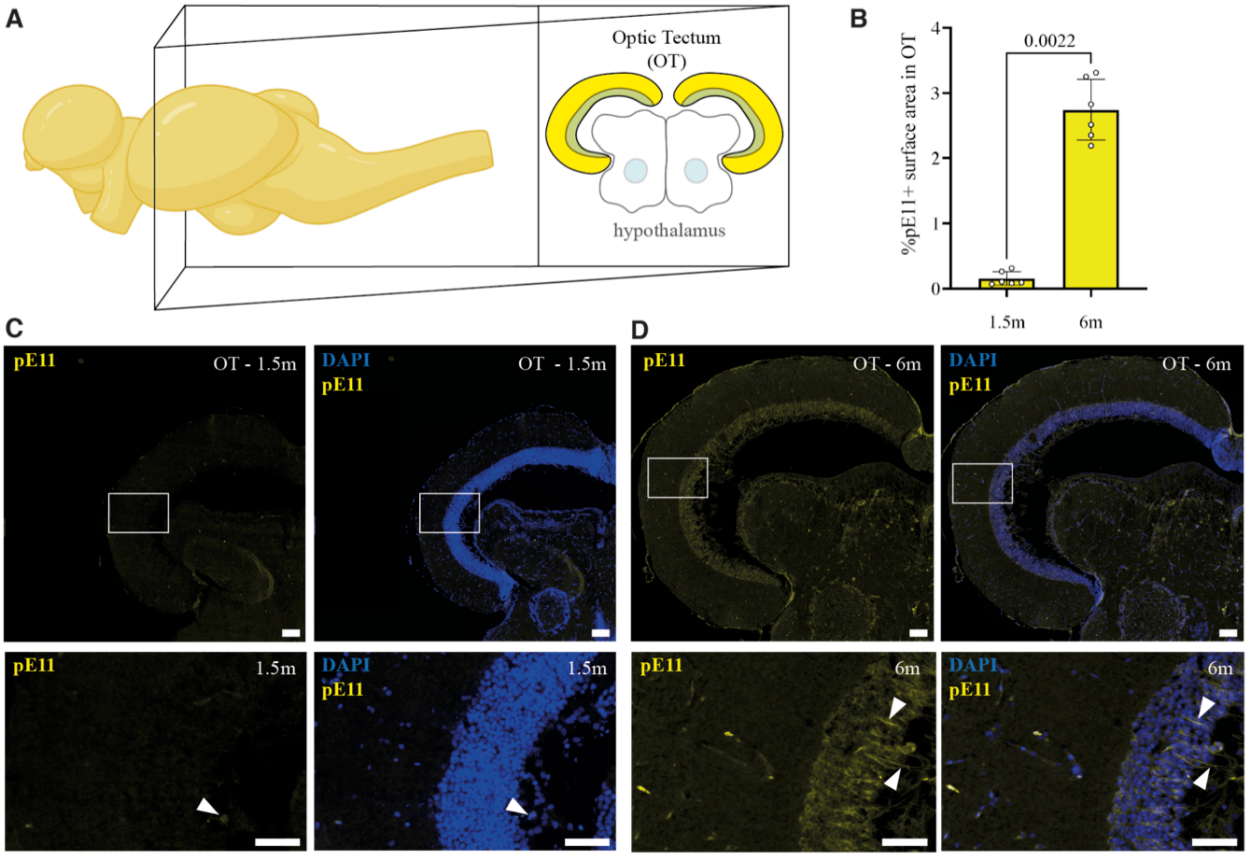

Figure S5. pE11 signal accumulates in the optic tectum in an age-dependent manner. (**A**) Schematic representation of the brain region quantified and shown in B-D. (**B**) Quantification of immunohistochemistry staining using the pE11 antibody on the optic tectum (TC) of young (6-week-old) and aged (6-month-old) killifish. Significance was calculated using a Mann-Whitney test. (**C, D**) Immunohistochemistry staining with the pE11 antibody (yellow) and DAPI (blue) in a 6-week-old (C) and 6-month-old (D) optic tectum. Arrowheads indicate regions with immunoreactivity. Scale bars represent 100 μm in the overviews and 50 μm in the zoom-ins.

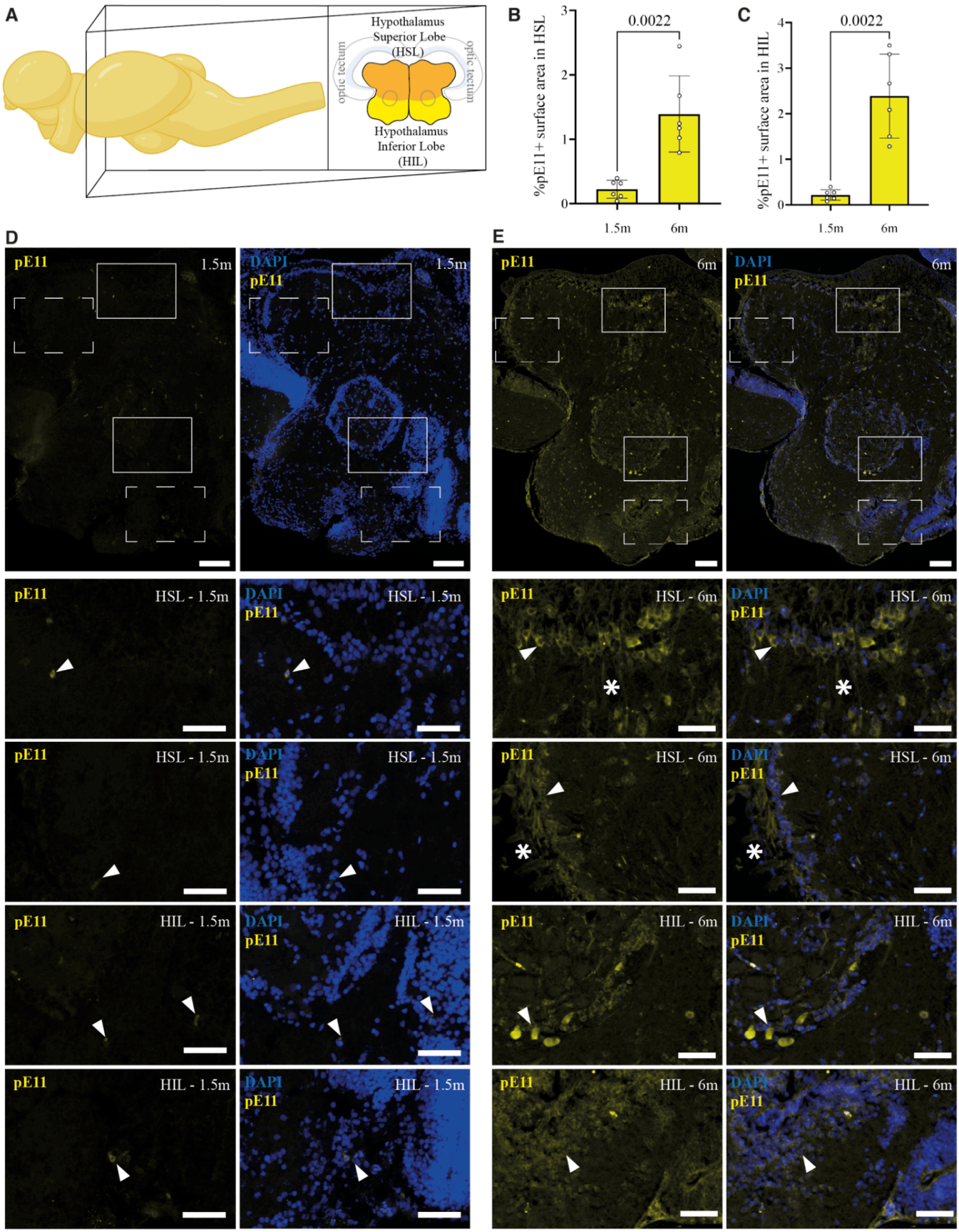

Figure S6. pE11 signal accumulates in the hypothalamus in an age-dependent manner. (**A**) Schematic representation of the brain regions quantified and shown in B-E. (**B,C**) Quantification of immunohistochemistry staining using the pE11 antibody on the hypothalamus superior lobe (HSL) and hypothalamus inferior lobe (HIL) of young (6-week-old) and aged (6-month-old) killifish. Significances were calculated using Mann-Whitney tests. (**D, E**) Immunohistochemistry staining with the pE11 antibody (yellow) and DAPI (blue) in 6-week-old (C) and 6-month-old (D) hypothalamus. Arrowheads indicate regions with perinuclear immunoreactivity. Asterisks indicate regions with filamentous immunoreactivity. Scale bars represent 100 μm in the overviews and 50 μm in the zoom-ins.

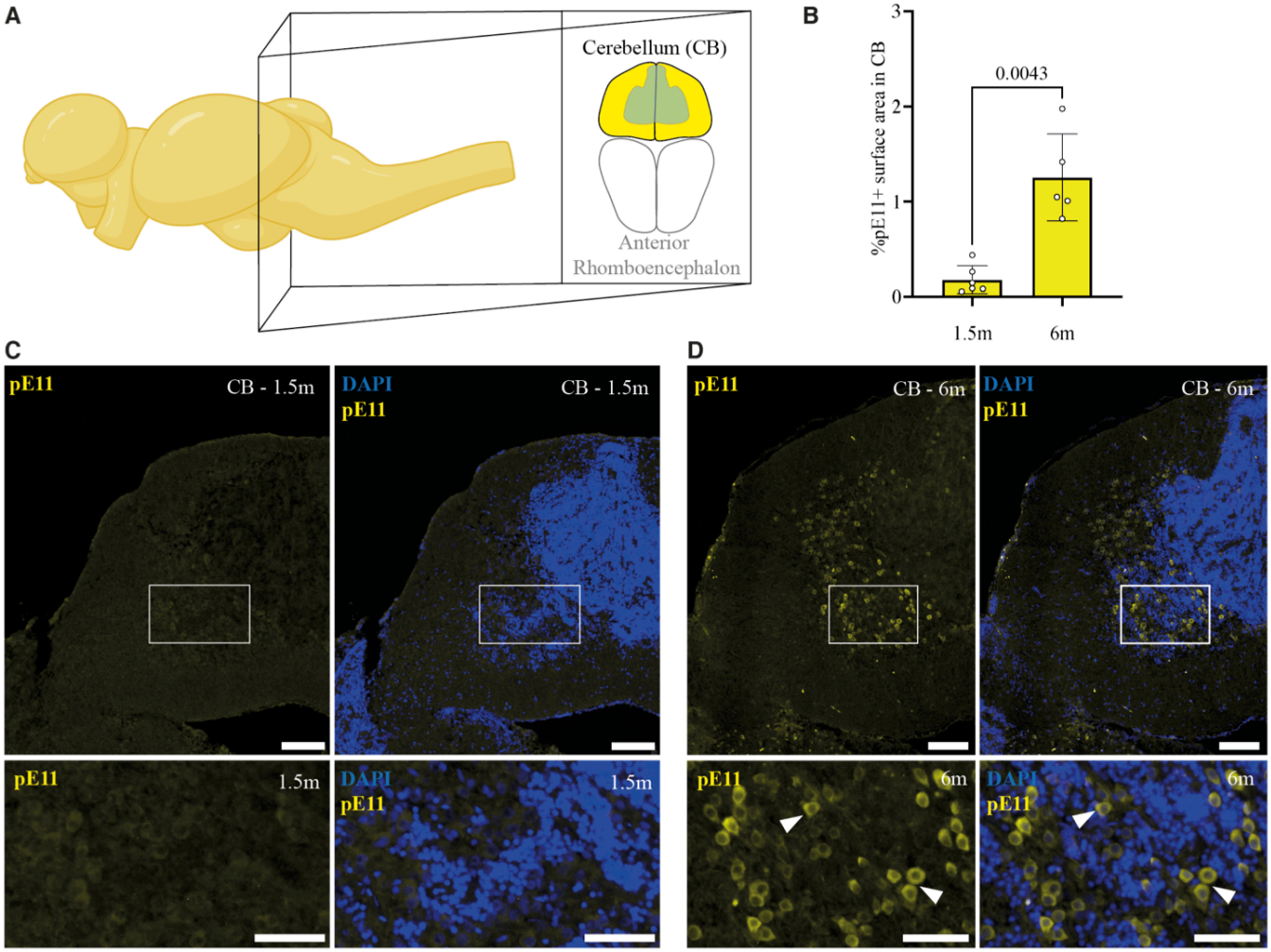

Figure S7. pE11 signal accumulates in the cerebellum in an age-dependent manner. (**A**) Schematic representation of the brain region quantified and shown in B-D. (**B**) Quantification of immunohistochemistry staining using the pE11 antibody on the cerebellum (CB) of young (6-week-old) and aged (6-month-old) killifish. Significance was calculated using a Mann-Whitney test. (**C, D**) Immunohistochemistry staining with the pE11 antibody (yellow) and DAPI (blue) in a 6-week-old (C) and 6-month-old (D) cerebellum. Arrowheads indicate examples of regions with perinuclear immunoreactivity. Scale bars represent 100 μm in the overviews and 50 μm in the zoom-ins.

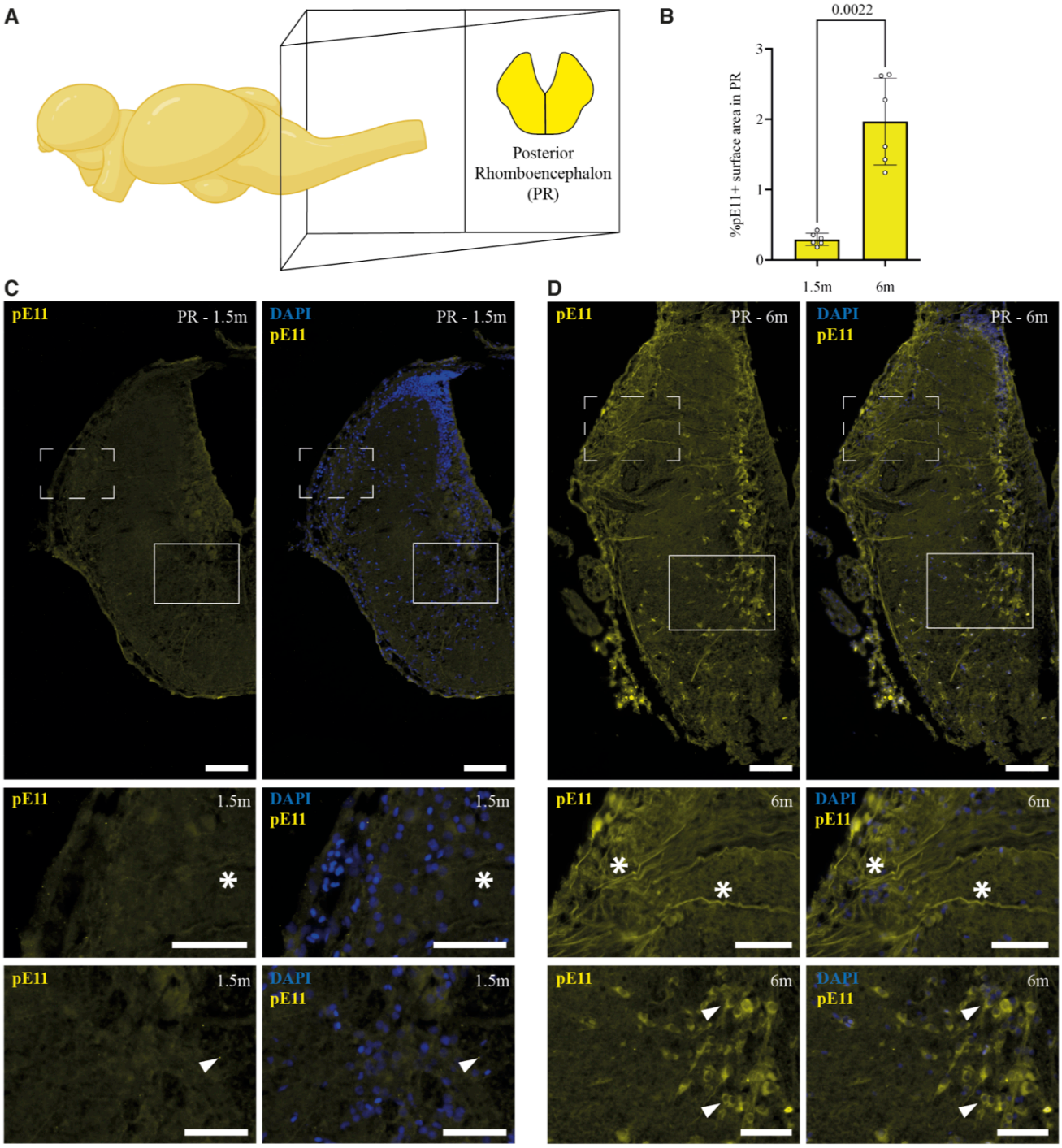

Figure S8. pE11 signal accumulates in the posterior rhomboencephalon in an age-dependent manner. (**A**) Schematic representation of the brain region quantified and shown in B-D. (**B**) Quantification of immunohistochemistry staining using the pE11 antibody on the posterior rhomboencephalon (CB) of young (6-week-old) and aged (6-month-old) killifish. Significance was calculated using a Mann-Whitney test. (**C, D**) Immunohistochemistry staining with the pE11 antibody (yellow) and DAPI (blue) in a 6-week-old (C) and 6-month-old (D) posterior rhomboencephalon. Arrowheads indicate examples of regions with perinuclear immunoreactivity. Asterisks indicate regions with filamentous immunoreactivity. Scale bars represent 100 μm in the overviews and 50 μm in the zoom-ins.

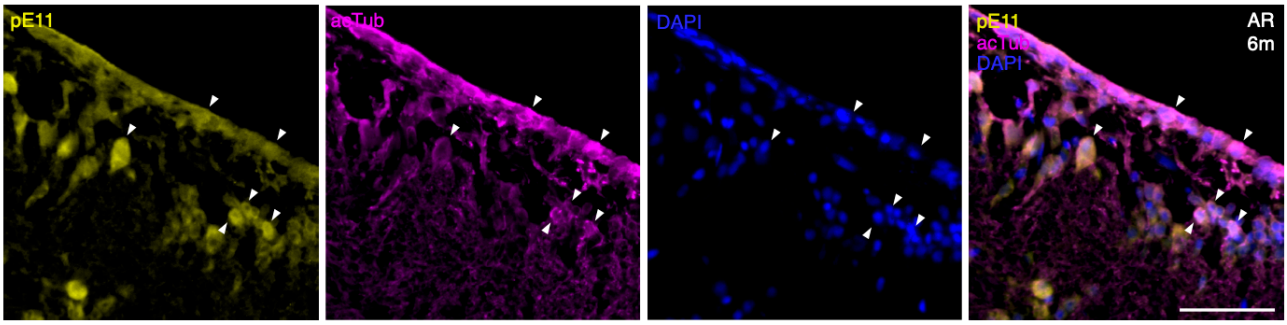

Figure S9. pE11 colocalizes with neuronal marker acTub. Immunohistochemistry staining using the pE11 and acTub antibodies, targeting $A\beta_{pE11}$ (yellow) and neuronal cytoplasm (magenta), respectively, in the anterior rhombencaphalon (AR) of a 6-month-old killifish. Scalebar represents 50 μm.

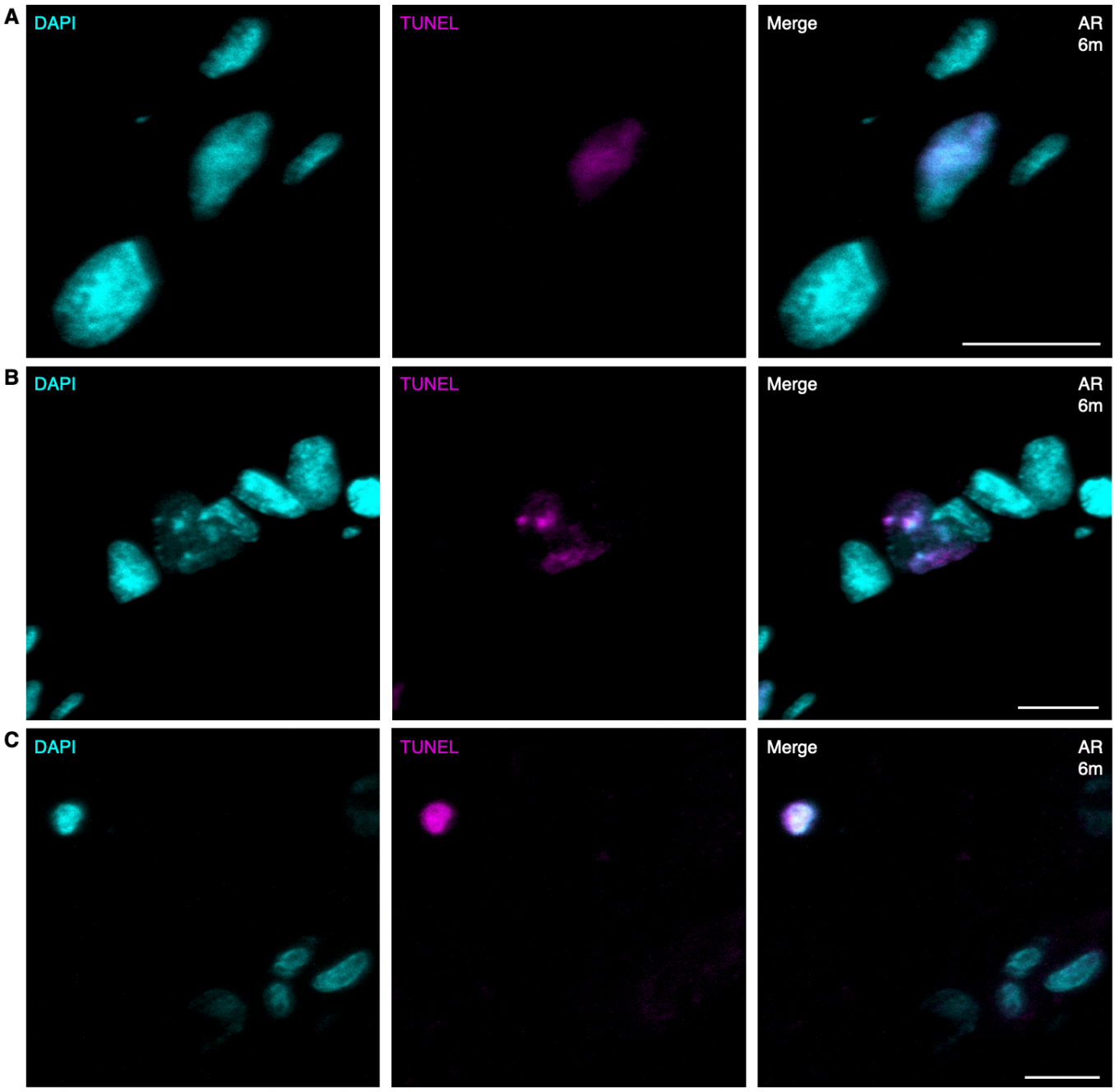

Figure S10. TUNEL staining in the anterior rhombencephalon. (**A-C**) Detection of apoptotic cells in the anterior rhombencephalon (AR) of a 6-month-old turquoise killifish through TUNEL staining. Various staining patterns were identified, including (**A**) visibly intact nuclei, (**B**) fragmented nuclei as well as (**C**) compacted nuclei. Scale bars represent 10 μm.

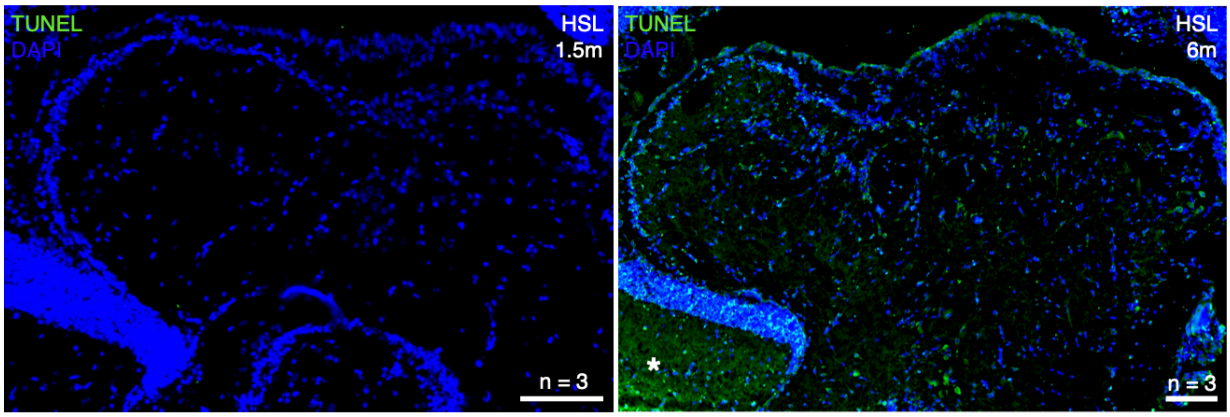

Figure S11. TUNEL staining is nearly undetectable in the hypothalamus of young turquoise killifish. Detection of apoptotic cells in the hypothalamus superior lobe (HSL) of a young 1.5-month-old (**left**) or aged 6-month-old turquoise (**right**) turquoise killifish, visualized through TUNEL staining (green). The asterisk indicates age-related background signal, which was consistent throughout the apical tip of the optic tectum throughout the investigated brain sections of 6-month-old fish. Scale bars represent 100 μm.

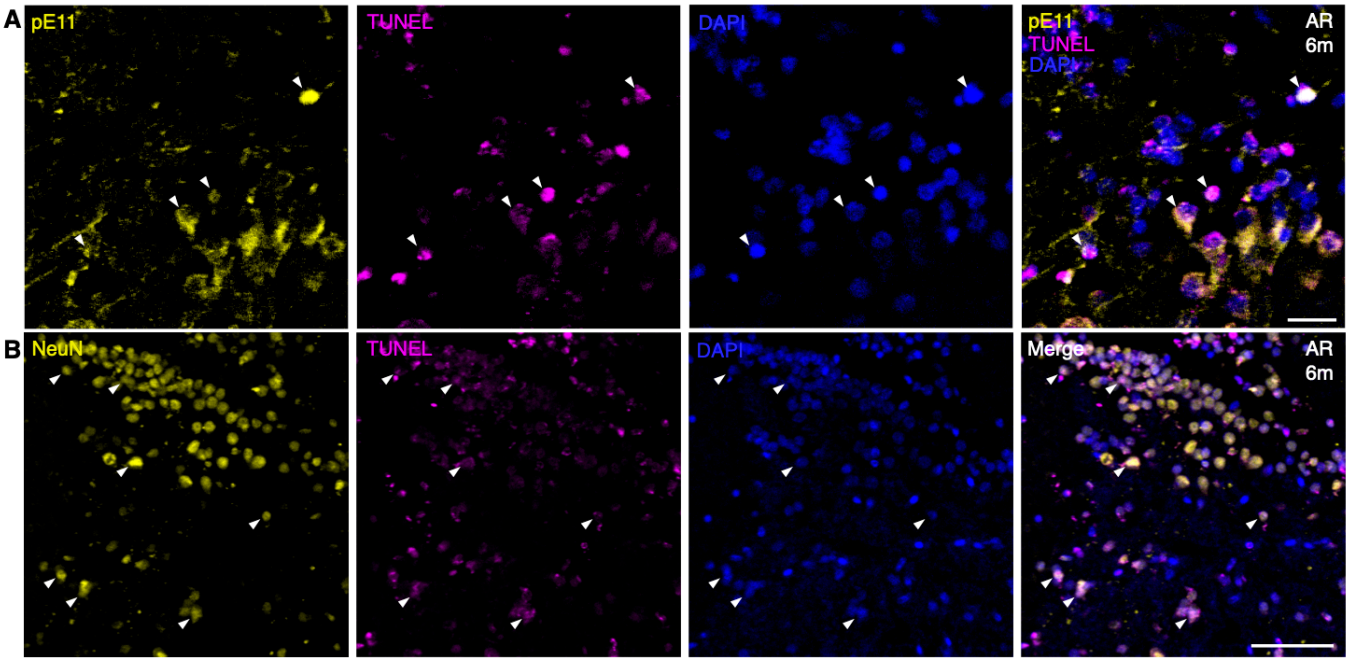

Figure S12. TUNEL staining colocalizes with pE11 and NeuN in the aged anterior rhombencephalon of the turquoise killifish. (**A**) Immunohistochemistry staining using the pE11 antibody (yellow) combined with TUNEL staining (magenta). Arrowheads indicate colocalizing signal. Scale bar represents 20 μm. (**B**) Immunohistochemistry staining using the pE11 antibody (yellow) combined with TUNEL staining (magenta). Arrowheads indicate overlapping signal. Scale bar represents 50 μm. (A,B) The stainings were performed on the anterior rhombencephalon (AR) of 6-month-old turquoise killifish.

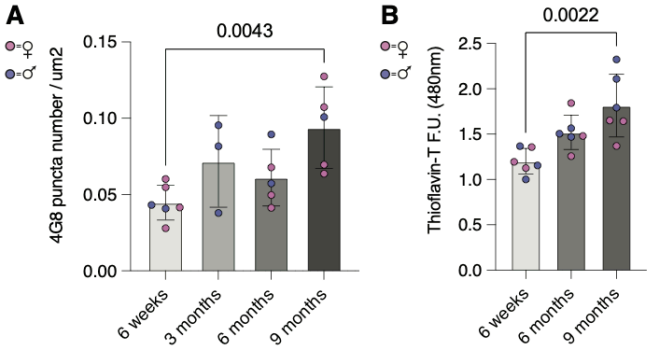

Figure S13. 4G8⁺ puncta and beta-sheet aggregates accumulate in an age-dependent manner. (**A**) Quantification of the number of 4G8⁺ puncta in the AR region at four different ages. Significance was calculated using a Mann-Whitney test. Error bars represent standard deviation. (**B**) Thioflavin-T assay was conducted on brain lysates of young, aged and old killifish. Shown values are 480nm emission levels 3 minutes after addition of Thioflavin-T to brain lysates. Values were normalized against the lowest measured value. Significance was calculated using a Mann-Whitney test.

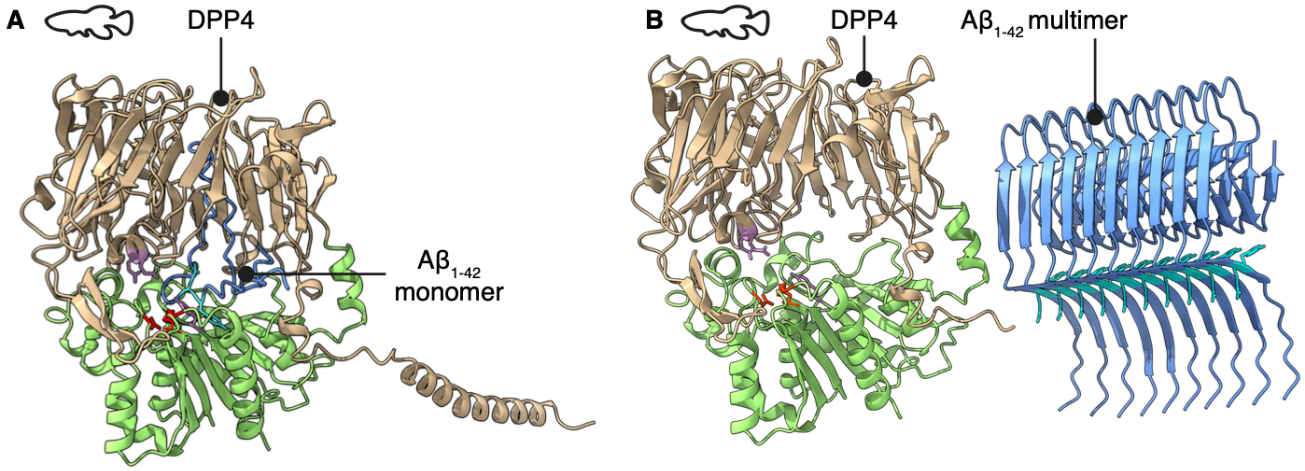

Figure S14. Killifish amyloid beta is unable to enter the molecular cleft of protease DPP4 while in an aggregated form. (**A**) Alphafold-predicted stucture shows that killifish amyloid beta monomers (*appa* derived) can occupy the molecular cleft of protease DPP4, which is known to truncate human amyloid beta allowing the formation of pyroglutamated amyloid beta. Beige indicates the predicted beta-propeller domain of DPP4, green indicates the hydrolase domain, red indicates the catalytic triade (S630, D708 and H740), dark blue indicates the amyloid beta (substrate) backbone, cleaved residues 10 and 11 are colored in lightblue, purple indicates residues supporting the positioning of the substrate in the catalytic core (Kirby et al. Clinical Science (2010) 118, 31–41). (**B**) Aggregated killifish amyloid beta ($A\beta_{1-42}$ multimer, *appa* derived) is unable to occupy the molecular cleft of DPP4, likely hampering the ability of DPP4 to truncate amyloid beta (coloring as in (A); flexible N-terminal part of the DPP4 beta-propeller domain not shown).

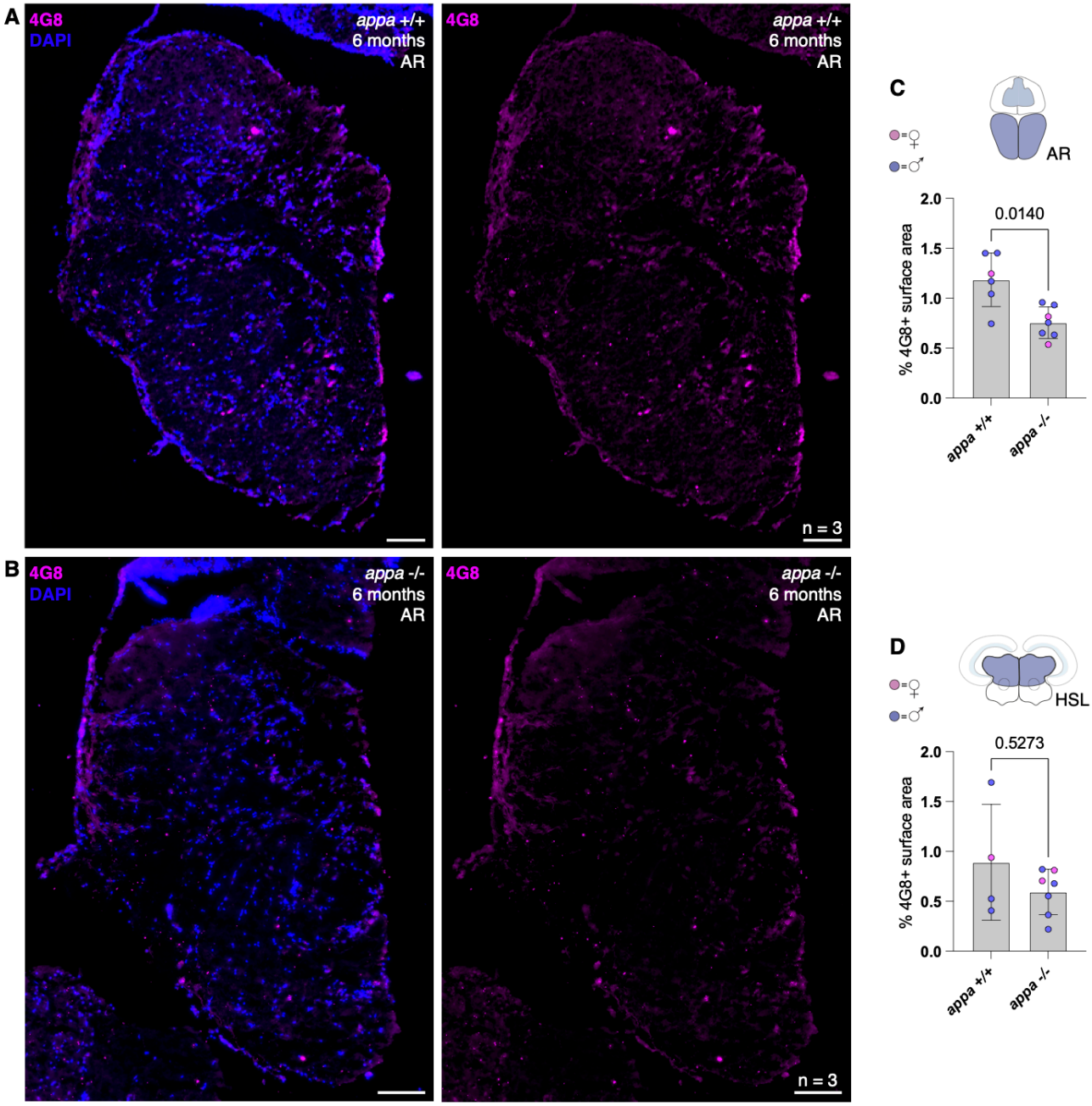

Figure S15. *appa* knock-out reduces 4G8 staining. (**A, B**) Representative immunohistochemistry staining results using the 4G8 antibody (magenta) in the anterior rhombencephalon (AR) of wild-type (A) and *appa* -/- mutant (B) brains. Scale bars represents 100 μm. (**C, D**) Quantification of the percentage of 4G8$^+$ covered surface area in the anterior rhomboencephalon (C) and hypothalamus superior lobe (D) of 6-month-old individuals. Significance was calculated using a Mann-Whitney test. Error bars represent standard deviation.

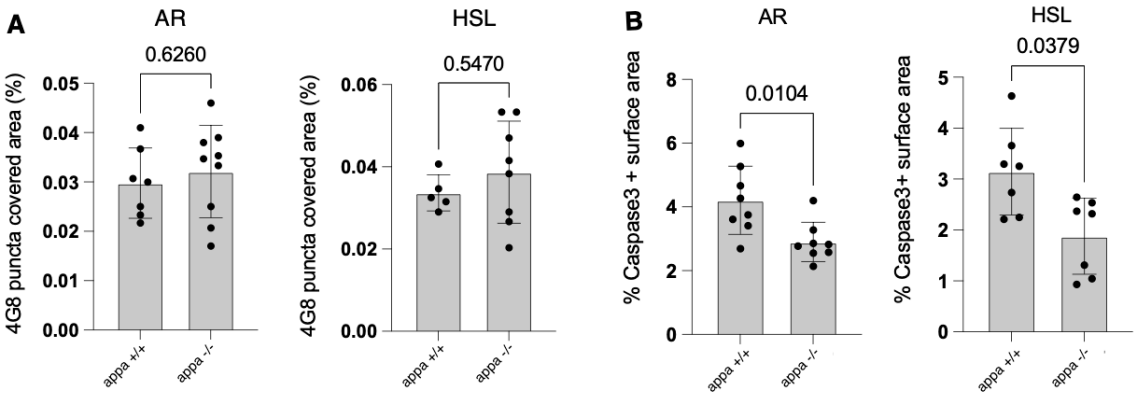

Figure S16. 4G8⁺ puncta covered surface area remains unchanged in *appa -/-* mutants, while showing a reduction in (pre)caspase3 covered surface area. (**A,B**) The percentage surface area covered by 4G8⁺ puncta (A) and (pre-)caspase3 (B) was quantified in the anterior rhombencephalon (AR) and hypothalamus superior lobe (HSL) of 6-month-old *appa -/-* mutants and their wild-type siblings. Significance values were calculated using Mann-Whitney testing.

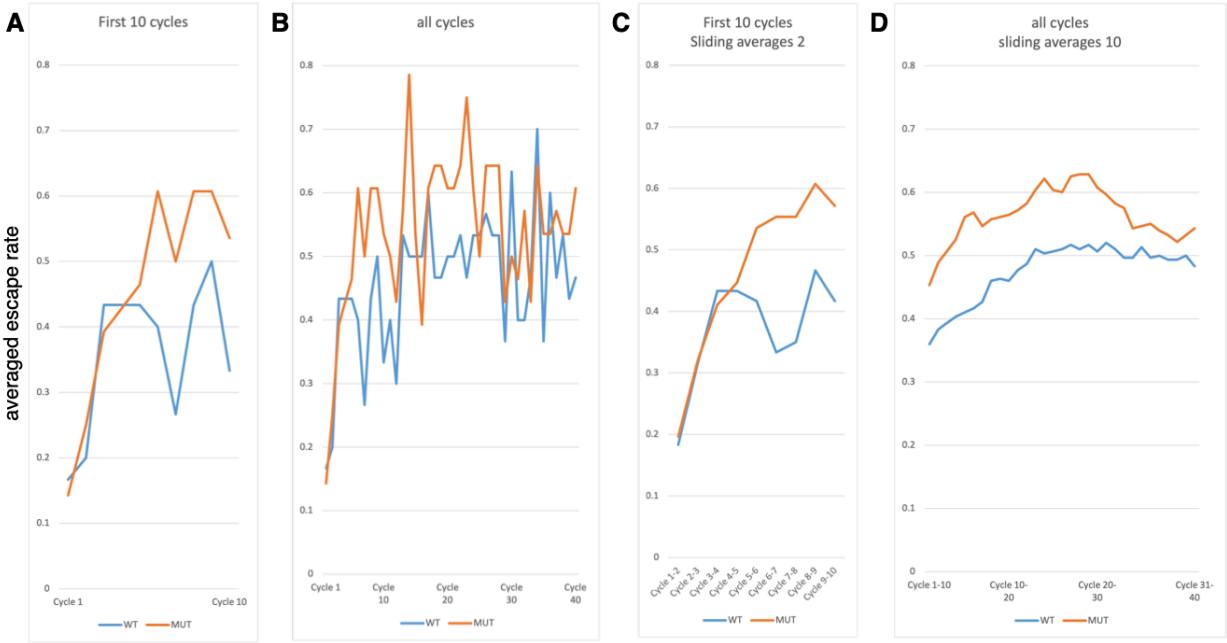

Figure S17. Averaged escape rates of *appa* -/- mutants and their wild-type siblings. (**A, B**) Plot describing the averaged escape rate of 7.5-month-old *appa* -/- mutants (orange, n = 28 fish) and their wild-type siblings (blue, n = 30 fish) across 10 (A) and the full 40 (B) cycles. (**C, D**) Sliding averaged values of the data presented in A and B, using either a sliding average of two (C) or ten (D) to increase the visibility of the general trends.

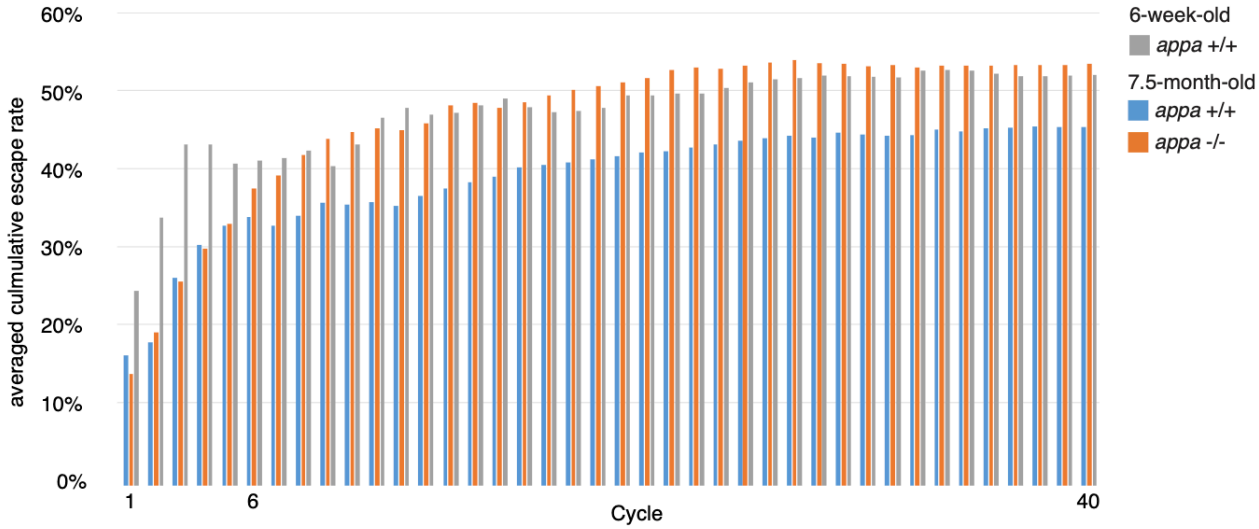

Figure S18. *appa* knock-out mitigates age-related learning deficiency in turquoise killifish. Plot describing the averaged cumulative escape rate of 7.5-month-old *appa* -/- mutants (orange, n = 28 fish) and their wild-type siblings (blue, n = 30 fish) across 40 cycles. In addition, a seperately conducted cohort of 6-week-old individuals has been tested and plotted (grey, n = 16 fish).